Clays and Clay Minerals, Vol. 64, No. 3, 245–274, 2016.

DIFFERENTIATING STYLES OF ALTERATION WITHIN KAOLIN-ALUNITE HYDROTHERMAL DEPOSITS OF ÇANAKKALE, NW TURKEY

HATICE ÜNAL ERCAN[1,3], Ö. IŞIK ECE[1,2,*], PAUL A. SCHROEDER[1,2], AND ZEKIYE KARACIK[1]

[1]Istanbul Technical University, Department of Geological Engineering, Maslak 34469 Istanbul, Turkey
[2]University of Georgia, Department of Geology, Athens, GA 30602-2501 USA
[3]Selçuk University, Department of Geological Engineering, Selçuklu 42250 Konya, Turkey

Abstract—The Biga Peninsula of NW Turkey is host to many kaolin and halloysite deposits with mineralization occurring at the intersections of fault zones in contact with Late Eocene–Miocene calc-alkaline volcanic rocks. Distinguishing between the relative overprinting of hypogene by supergene processes in these deposits is a challenge and important because they affect the physical-chemical properties of minerals and their potential for industrial applications. This study examines the Sarıbeyli-Sığırlı and Bodurlar kaolin deposits in NW Turkey, which were formed from similar volcanics as evidenced by $^{40}Ar/^{39}Ar$. Late Eocene (34.2 ± 0.20 Ma) to Early Oligocene (32.7 ± 0.17 Ma) ages for both primary volcanic rocks and alunites are consistent with surrounding rocks in the Çanakkale region. Criteria used to distinguish hypogene alteration from supergene alteration processes come from X-ray diffraction (XRD), Fourier-transform infrared (FTIR) and Raman spectroscopies, thermal gravimetric analysis (TGA), scanning and transmission electron microscopy (SEM, TEM), and elemental analyses. Isotopic $\delta^{18}O$ depletion and δD enrichment of the Sarıbeyli-Sığırlı deposit suggests that it was more influenced by magmatic waters than was the Bodurlar deposit. The Bodurlar deposit contains a paucity of dickite compared to the Sarıbeyli-Sığırlı deposit, which is evidenced by lower TGA endotherms, higher ratios of XRD intensities for reflections at 1.316 Å and 1.307 Å, distinctive FTIR absorbance bands at 3620 cm^{-1} and 3652 cm^{-1}, and relative Raman intensities of the ν_1 and ν_5 vibrational modes.

A genetic model is proposed whereby these deposits are mainly formed through an acid-sulfate hydrothermal alteration, in what appears to be a volcanic-hydrothermal system. The extent of hydrothermal alteration was controlled by fault density and the initial texture of the volcanic rocks. These steam-heated environments included sulfide-enriched vapors and groundwater mixed to varying degrees in the vadose zone. The Sarıbeyli-Sığırlı and Bodurlar deposits, respectively, contain mineral assemblages that reflect both hypogene (kaolinite, alunite, dickite) and supergene (kaolinite, halloysite, jarosite) processes. These observations offer a basis for comparing and discriminating the relative influence of these two important alteration processes responsible for the formation of kaolin deposits in NW Turkey and around the world.

Key Words—Alterations, Alunite, Ar-Ar dating, Çanakkale, Halloysite, Hydrothermal, Hypogene, Supergene, Kaolinite, O, H, and S isotopes, Turkey.

INTRODUCTION

The Biga Peninsula, where hydrothermal alterations dominate, is one of most tectonically active regions of Turkey. It is a part of the Tethyan Metallogenic Belt extending from Switzerland to Iran. As a result of active tectonism and hydrothermal alterations, this region is considered to be one of the richest areas with regard to metallic and industrial mineral deposits in Turkey. Many active mines are present in the Biga Peninsula, including some near the study area such as the Halilağa-porphyry Cu mineralization, and the Ağıdağı and Kirazlı high sulfidation (HS) epithermal mineralizations that are the most important examples currently producing Au, Ag, Mo, and Cu (Yiğit, 2012). Moreover, kaolin is the most abundant industral raw material produced in the Biga Peninsula.

* E-mail address of corresponding author:
ece@itu.edu.tr
DOI: 10.1346/CCMN.2016.0640305

Economically important kaolins in northwestern Turkey occur as (1) primary deposits derived from acid-sulfate hydrothermal alteration of volcanic rocks (Arslan *et al*., 2006; Ece and Schroeder, 2007; Ece *et al*., 2008, 2013; Kadir *et al*., 2011; Acarlıoğlu *et al*., 2012), (2) secondary kaolin deposits derived from lacustrine deposits formed by weathering of volcanic rocks with andesitic composition and subsequent transportation and deposition processes (Ece *et al*., 2003), and 3) *in situ* weathering products on the granodiorite complex (Bilecik-Söğüt) (Kadir and Kart, 2009). These kaolins are used mainly in the ceramic, porcelain, paper, and plastics industries (Murray, 2000; Kadir and Akbulut, 2009). Understanding the origins and variations of kaolin crystal chemistry are important factors for future exploration and exploitation of these deposits.

All previous geological studies in and around the study area concentrated on the metallic mineral reserves of the region. Yiğit (2012) investigated the reserves of potential metallic ore deposits of the Biga Region and summarized the relationships between alteration zones

and regional volcanism using geochronological data from fresh and altered volcanic rocks. In this study, the Bodurlar kaolin quarry's mineral assemblage of native sulfur, vuggy quartz, alunite, and pyrophyllite was described as an HS epithermal system. No detailed mineralogical studies have been done for the alteration zones of both the Bodurlar and Sarıbeyli-Sığırlı kaolin deposits, and the origin of geothermal solutions responsible for the hydrothermal alterations has not been investigated to date.

The mechanism most responsible for the creation of kaolin is a hydrolysis reaction driven by acidic waters generated either at high temperatures (>60ºC) by reacting sulfuric compounds or at low temperature (<60ºC) by reacting organic and carbonic acids (Murray *et al.*, 1993; Hurst and Pickering, 1997) and oxidizing Fe sulfides. The rate of formation and abundance of kaolin deposits is generally thought to increase with geologic time and be globally controlled by climate, tectonics, crustal differentiation, and biology (Schroeder and Erickson, 2014). These kaolin deposits are found at or near the Earth's surface today. Such deposits have experienced thermal, chemical, and burial changes that require characterization.

A clearer picture of the mineralization processes responsible for the formation of a kaolin deposit provides a better means to selectively exploit it, so as to minimize energy and environmental effects and maximize ore production for its intended application (Kogel, 2014). In practice, many primary kaolin deposits are formed by episodic and multi-causal reaction events that may involve both magmatic and meteoric waters.

The goal of the present study was to improve criteria for distinguishing kaolin deposits that have been affected by both hypogene and supergene processes. The crystal-chemical properties of two kaolin deposits in the Çanakkale Province of NW Turkey that are close to each other in apparently similar geologic environments, influenced by both magmatic and meteoric waters, were compared and contrasted. This region lent itself well to identifying the imprints of these processes because it is composed of volcanic rocks of variable permeability in a tectonically active area, where extensional horsts and graben resulted in localized steep geothermal gradients (relatively high heat flow) along fault zones. Near-surface exhumation of kaolin deposits by faulting (and subsequent exposure by mining), combined with the frequency of flushing events and water flow rates at different intensities and volumes of geothermal water, provided an opportunity to examine the distinct differences in crystal- chemical characteristics recorded in the rocks.

GEOLOGIC SETTING

The Çanakkale Province is located on the Biga Peninsula and is a well-known natural resource area in Turkey for industrial minerals, dimension stone, energy raw materials, precious stones, and base metals (Yiğit, 2006). Epithermal systems throughout the peninsula contributed to the genesis of some of these economic deposits, which historically have been developed over a range of low-sulfidation to high-sulfidation conditions (Ağdemir *et al.*, 1994; Yiğit, 2009). Most of these epithermal deposits are hosted in the andesitic lavas and related pyroclastic deposits emplaced during the Oligo-Miocene convergent margin events (Aldanmaz *et al.*, 2000). Geological and tectonic evolution of the region has led to the formation of complex volcanic structures and related porphyry and epithermal systems. Hydrothermal acid-sulfate alteration resulting in halloysite and alunite occurrences were reported by Ece *et al.* (2008), who used mineralogical, geochemical, and isotopic data to support the hypothesis that the presence of H_2SO_4 enhanced the acidity in hydrothermal solutions that led to advanced argillic alteration.

Many examples of high- and low-sulfidation epithermal systems occur around the world that are similarly hosted by calc-alkaline volcanics, such as in Sardinia, Italy, in Matsukawa, Japan, and in Simav, Turkey (Nakamura *et al*., 1970; Heald *et al*., 1987; Simón *et al*., 2005; Ece *et al*., 2013). Kaolinite, silica minerals, and alunite are commonly associated with advanced argillic alteration. The extent to which the mineral assemblages in these deposits formed in hypogene *versus* supergene environments is still poorly understood (Dill *et al*., 1997, 2015; Ece *et al*., 2008, 2013), particularly in the Biga Peninsula region.

The Sarıbeyli-Sığırlı and Bodurlar kaolin deposits in the Biga Peninsula region appear to be similar to other epithermal deposits (Kirazlı, Dede Dağı, and Çaltıkara high-sulfidation) (Yiğit, 2012) and despite being economically important, their origins have not been extensively studied. This study provides an opportunity to compare the mineralogical and isotopic properties of these two Biga Peninsula deposits with other epithermal systems around the world. The hypothesis is that the Sarıbeyli-Sığırlı and Bodurlar kaolin deposits are overprinted by hypogene and supergene processes and that radiometric ages, stable-isotope compositions, and mineralogy will give insights into the timing and extent of these events. A conceptual geologic model is proposed to explain the origin of these deposits that can be compared with other epithermal systems and provide criteria for distinguishing magmatic from high-temperature and low-temperature epithermal processes in the kaolin deposits.

The Sarıbeyli-Sığırlı and Bodurlar deposits comprise Oligocene-Miocene volcanic and intrusive rocks (Figure 1). Magmatism was derived from the subduction of the northern branch of the Neo-Tethyan Ocean related to collisional movement of the African-Arabian plate (Şengör, 1979; Şengör and Yılmaz, 1981). The volcanic rocks that cover the region extend from Edremit to

https://doi.org/10.1346/CCMN.2016.0640305 Published online by Cambridge University Press

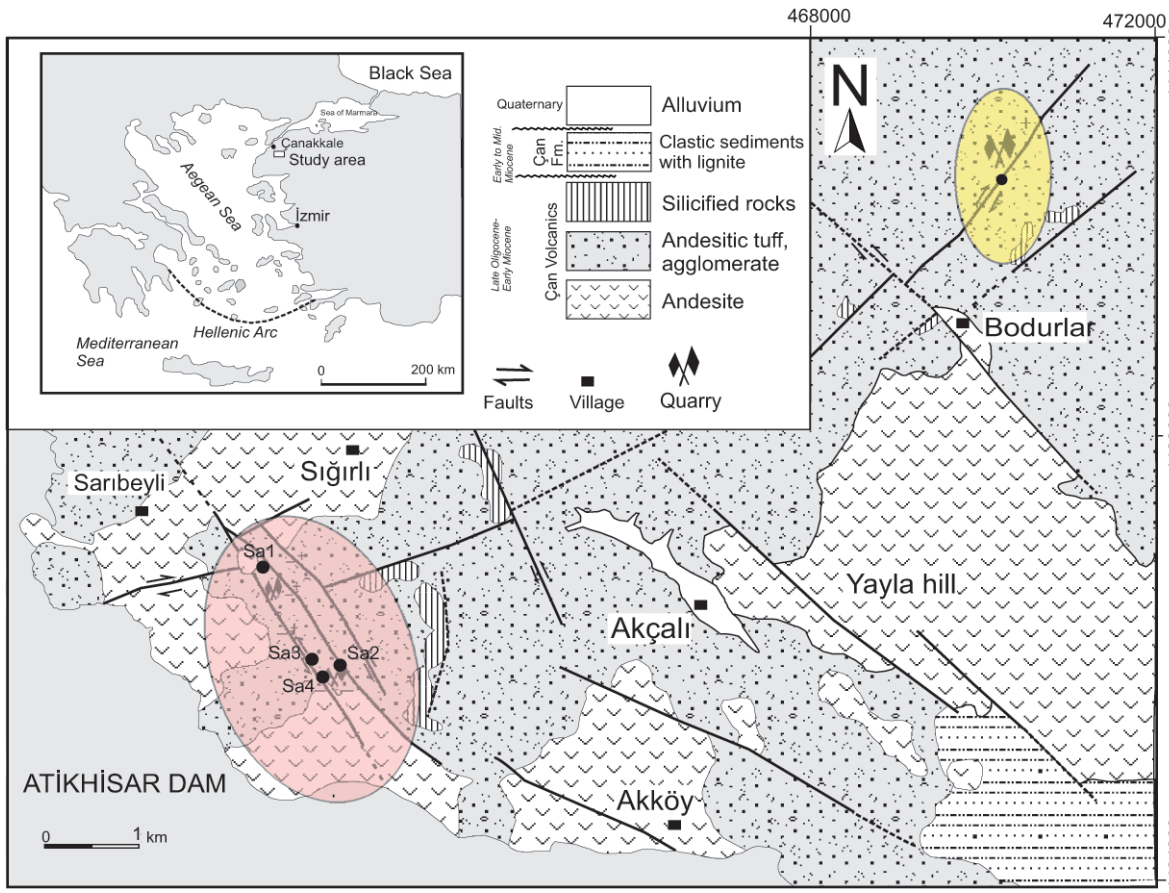

Figure 1. Simplified geologic map of the study area. Upper inset map indicates the location of Western Turkey and neighboring regions. Reddish and yellowish (colors refer to the online version of this paper) regions at lower left and upper right indicate approximate areas shown in the detailed geologic maps found in Figure 2 (Sarıbeyli-Sığırlı area) and Figure 3 (Bodurlar area), respectively.

Çanakkale to the eastern Aegean Islands (Yılmaz, 1990; Seyitoglu and Scott, 1992; Birkle and Satır, 1995). Two geochemically distinct volcanic rock suites in the Biga Peninsula include a calc-alkaline and an alkaline series (Yılmaz, 1990).

The calc-alkaline andesitic volcanics that crop out in the Gökçeada, Edremit, and Çan areas are collectively referred to as the Çan volcanics (Ercan *et al*., 1995; Kaymakcı *et al*., 2007). These rocks have reported radiometric ages ranging from 23.6 ± 0.6 to 34.3 ± 1.2 Ma (Krushensky, 1975; Ercan, 1979; Altunkaynak and Genç, 2008; Yiğit, 2012). They are spatially associated with older Eocene granitoids in the region. Upper Miocene–Pliocene conglomerates, claystones, siltstones, and lignites unconformably overlie the Çan volcanics (Dayal, 1984; Delaloye and Bingöl, 2000; Karacık *et al*., 2008).

Rocks in the Çan volcanic suite are classified as porphyritic andesite, basaltic-andesite, and basaltic-trachyandesite that display porphyritic textures. They consist mainly of plagioclase, clinopyroxene, hornblende, and biotite with secondary alteration minerals such as carbonate and clay. Biotite- and hornblende-bearing rocks are sometimes altered to Fe-bearing chlorite and Fe-(oxyhydr)oxide minerals. Tuffs are primarily composed of plagioclase and biotite microcrystal fragments in an ash matrix. Lithological characteristics of tuffs vary over a short distance from ash to lapilli and blocky tuffs.

The Sarıbeyli-Sığırlı kaolin deposit occurs in volcanic rocks of Oligocene age in a zone bounded by two NW–SE trending strike-slip faults (Figure 2). It was exposed in four open pits between two fault zones (F1 and F2). The mineral assemblages of the deposits are similar, but their relative abundances differ (details are explained in the following sections). The four subdeposits were named after the locations in the mining site and are labeled Sa1, Sa2, Sa3, and Sa4 in Figure 2. Field relationships suggest that faults F1 and F2 likely served as the conduits for ascending hydrothermal fluids. Fractures within the tuffs appear to have controlled access of hydrothermal solutions, which were differentially infiltrated depending on porosity and permeability. The Sa1 is located between F1 and F2, but Sa2 pits are located along F1; Sa3 and Sa4 pits are associated with F2. The Sa1 pit covers an area of 1.125 km^2, while the

https://doi.org/10.1346/CCMN.2016.0640305 Published online by Cambridge University Press

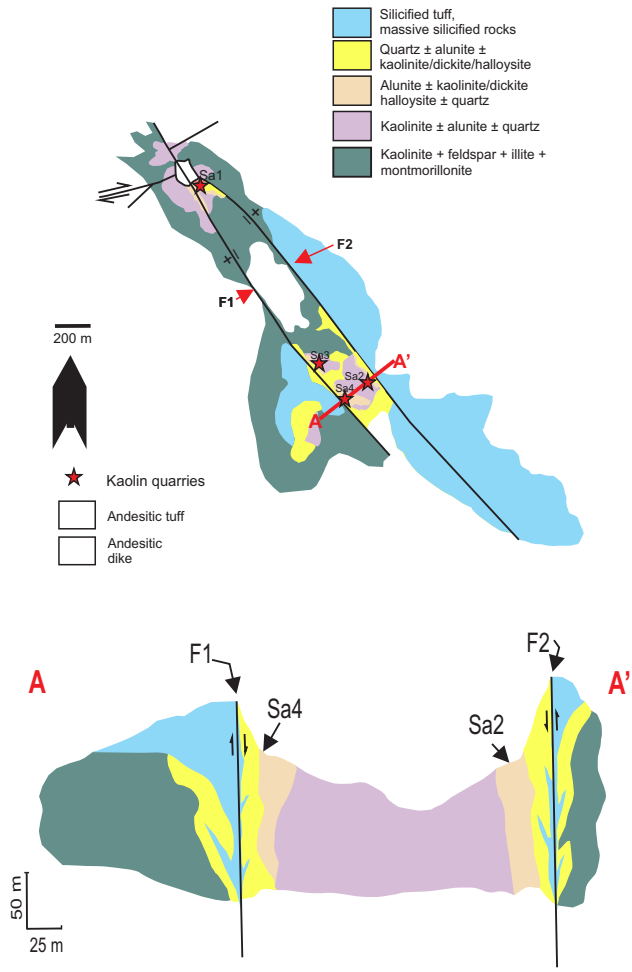

Figure 2. Upper part: Geology and alteration map of the Sarıbeyli-Sığırlı epithermal system. F1 and F2 show fault zones and relative displacement (+/−). Sa1, Sa2, Sa3, and Sa4 indicate open-pits of the Sarıbeyli-Sığırlı deposits. Lower part: Schematic section through the Sarıbeyli-Sığırlı epithermal field, showing alteration zonation at two of the studied sites. Arrows indicate displacement directions along faults.

other three sites (Sa2, Sa3, and Sa4) are located close together and partially overlap to cover an area of ~1.2 km^2 (Figure 2 lower).

The Bodurlar deposit also occurs in the Oligocene volcanic rocks dominated by andesitic lavas and tuffs (Figure 3) and covers an area approximately 2 km^2 with six fracture zones filled with silicified rocks. Lithological properties of Bodurlar volcanics are similar to the Sarıbeyli-Sığırlı deposit. Kaolinization occurs within massive white- and purple-colored tuffs with plagioclase and biotite fragments in the ash matrix. The blocks consist mainly of andesitic lavas and tuffs. The main tectonic features of the Bodurlar deposit are NE-trending faults. Six silicified fracture zones (labeled F1 to F6 in Figure 3b) occur within the same wide flower-like fault zone that passes through the kaolin deposit along which ascending hydrothermal fluids are believed to have moved.

The top-down appearance of the exposed high wall in the pits also bears evidence of a meteoric weathering front that is dominated by iron (oxyhydr)oxide staining. Appearance alone, however, does not allow for distinguishing the extent of high and low temperature alteration and the relative contributions of meteoric *versus* magmatic water sources.

METHODS

Field observations and geological mapping were first performed to characterize the area in more detail, with sampling limited to outcrops and open pits. Petrological properties of collected samples were determined using thin-section petrography and X-ray diffraction (XRD), at Istanbul Technical University (ITU). Fifty thin sections were examined using a Leica DM4500P polarizing microscope and 99 samples were analyzed using a

https://doi.org/10.1346/CCMN.2016.0640305 Published online by Cambridge University Press

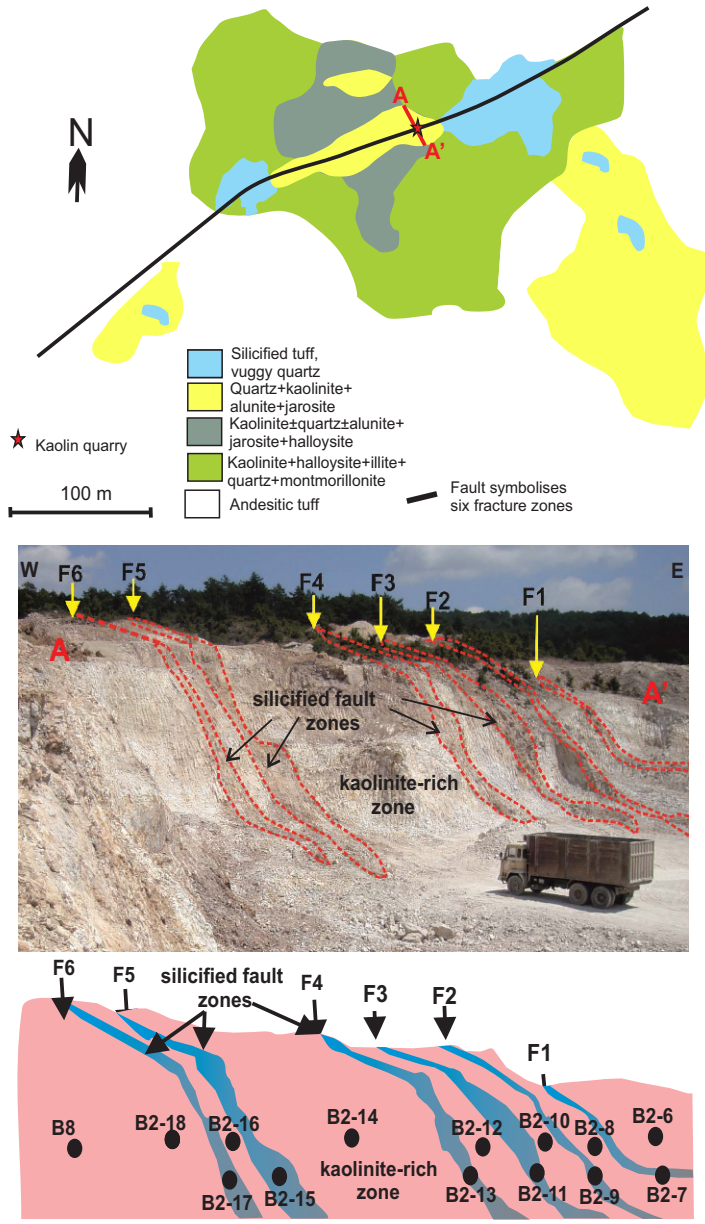

Figure 3. Upper part: Geologic and alteration sketch map of the Bodurlar epithermal system. Middle part: Photo showing wide fault zone with six siliceous veins. Lower part: Schematic section through the Bodurlar deposit, showing alteration zones, sample numbers, and locations.

Bruker D8 Advance diffractometer. XRD data were collected using CuKα radiation (40 mA, 40 kV), scanning range of 2–72º2θ, and step-size of 0.01940º for bulk random mounts, and 2–42º2θ, and step size of 0.005º2θ for oriented mounts, 0.1 sec/step, 0.2 mm divergence slit, Ni filter, and a LynxEye® solid-state detector. The kaolin samples were ground for XRD analysis using a Retsch RM 200 tungsten carbide grinding mill to reduce the particle-size to <10 μm. Samples were shaken mechanically in distilled water to disperse as much clay-size material as possible. Size fractionation of the clays (<2 μm equivalent spherical diameter) was performed using a Beckman Coulter Aventi J-E super centrifuge. After decanting the supernatant liquid and homogenization of the clay paste, oriented clay mounts were prepared by smearing on glass slides. These slides were examined by XRD as air-dried, ethylene glycol solvated for at least 16 h at 60ºC,

https://doi.org/10.1346/CCMN.2016.0640305 Published online by Cambridge University Press

Table 1. Chemical compositions of the Sarıbeyli-Sığırlı kaolin deposit. Abbreviations: al: alunite, ka: kaolinite.

%	SA2-12 al	SA2-10 al	SA2-19 al	SIG-3-4 al	SIG-3-3 al	SA1 al	SIG-2-5 ka	SA2-22 ka	SA2-20 ka	SIG-3-6 ka	SIG-2-6 ka	SA2-27 ka	SIG-3-2 ka	SIG-2-5K ka	SA4 ka	SA2-26 ka	SIG-2-2 ka
SiO_2	7.50	5.74	11.29	13.94	25.64	21.25	39.85	42.94	41.06	40.66	30.49	42.41	43.12	43.87	41.24	41.93	46.90
Al_2O_3	41.50	44.51	38.22	41.77	38.36	40.85	39.79	39.22	37.23	39.95	48.04	38.51	39.85	39.50	40.55	39.01	24.70
Fe_2O_3	1.17	0.14	1.17	0.37	0.26	0.13	0.60	0.14	0.07	0.21	0.16	0.75	0.03	0.12	0.04	0.09	0.13
CaO	0.06	0.06	0.04	0.09	0.13	0.10	0.17	0.06	0.02	0.08	0.11	0.07	0.04	0.07	0.12	0.08	0.04
Na_2O	0.48	0.67	0.47	0.82	0.76	1.30	0.04	-	0.14	0.07	0.08	–	–	0.03	–	0.04	0.31
K_2O	8.49	8.74	6.58	6.40	4.45	3.99	0.07	0.07	1.55	0.45	0.27	0.05	0.08	0.05	0.03	0.08	4.68
TiO_2	0.49	0.14	1.09	0.59	0.68	0.44	0.38	0.55	0.75	0.67	0.64	1.43	0.65	0.83	0.14	1.34	0.62
P_2O_5	0.38	0.42	0.34	0.61	0.69	0.50	1.07	0.50	0.21	0.81	0.77	0.43	0.33	0.23	0.70	0.62	0.27
LOI	39.47	39.06	38.11	34.83	28.39	30.91	15.32	14.91	18.36	16.10	16.26	14.88	14.75	14.62	15.11	14.88	22.06
Total	99.53	99.48	97.31	99.42	99.35	99.47	97.28	98.39	99.38	99.01	96.82	98.54	98.86	99.32	97.95	98.06	99.71
ppm																	
Au	6	0.9	3.9	1.3	1.7	–	–	2.1	–	–	2.8	9.6	–	1.3	1.6	–	–
Ag	–	–	42	–	–	–	–		–	36	–	–	–	–	–	–	–
As	75	6.5	183	108	88	41	74	7	187	61	58	157	19	2.3	2.7	–	–
Ba	1101	1511	1206	1308	1290	1102	2552	613	2134	1844	2084	494	384	1128	7060	927	672
Ce	44	35	46	84	100	–	–	64	–	–	72.5	86	–	82	27	–	–
Cl	67	–	26	160	174	133	–	121	251	124	113	126	–	103	96	99	90
Cu	51	22	72	58	34	24	122	4.3	68	56	38	56	21	20	25	16	24
Ga	24	138	29	22	32	22	81	63	159	94	50	55	61	41	111	94	18
Hf	2.7	1	5.9	3	3.2	–	–	2.9	–	–	3.1	6.7	–	9.6	0.6	–	–
Hg	0.89	0.22	0.88	0.03	0.03	–	0.19	0.03	–	0.11	0.33	0.07	0.03	0.19	0.02	–	–
La	25.5	26	27.2	47	56	–	–	45	–	–	41.3	48	–	52	20	–	–
Mo	7	5	–	–	3	–	–	–	–	5	–	2.8	10	12	–	–	–
Nb	3.3	1.7	10	4.2	6.1	–	–	3.9	7	–	7.1	6	–	18	1.2	–	–
Nd	13	26	16	26	33	–	–	20	–	–	26.6	34	–	24	7.4	–	–
Ni	–	–	–	–	12	–	13	–	15	15	10	–	–	–	12	–	14
Pb	123	294	145	116	159	95	242	779	374	91	194	403	47	200	664	589	168
Pd	45	–	–	–	–	–	–	–	–	30	36	–	–	–	–	45	–
S	–	–	–	–	–	–	5609	3223	–	–	8632	2802	2795	1109	3833	4126	–
Sb	126	0.9	19	10.4	2.8	–	–	1	–	–	3.7	11	–	0.4	0.9	–	–
Sr	1823	1754	2265	2486	3053	2915	7197	4553	1320	4585	5808	4047	1978	1563	4858	4952	1247
Th	11	5.1	11	12.5	13.5	17	–	2	3	21	15	17	–	28	5.1	20	–
V	331	375	342	331	318	–	547	305	–	757	439	404	598	138	216	376	–
Y	2.8	1.3	6.4	5.5	4.7	–	–	4.9	–	–	3.3	9.7	–	16	1.3	–	–
Zn	–	–	–	1	14	–	–	–	–	–	–	9	–	–	–	–	10
Zr	194	138	223	238	271	218	167	283	376	227	261	436	262	727	114	444	257

heated at 400ºC for 1 h and 550ºC for 30 min, according to Moore and Reynolds (1989).

Whole-rock chemical analyses (Table 1 and Table 2) were performed at Acme Labs, Canada, using DS9, DS10, GGC-02, GS311-1, GS910-4, and SO-18 international standards. Major and trace elements were analyzed using Spectro Ciros Vision inductively coupled plasma optical emission spectroscopy (ICP-OES) for Ba and Sc (0.2 g pulp sample by $LiBO_2$ fusion) and Mo, Cu, Pb, Zn, Ni, and As (0.5 g sample leached with 3 mL of 2-2-2 HCl-HNO_3-H_2O at 95ºC for 1 h, diluted to 10 mL). A Perkin-Elmer Elan 6100 inductively coupled plasma mass spectrometer (ICP-MS) at ITU was used for other trace and rare earth elements (*REE*).

Sixteen clay and alunite-bearing samples were examined for morphological properties using a JEOL JSM-7000F field emission scanning electron microscope (FE-SEM) (Bozzola and Russell, 1999) at ITU, Department of Materials Engineering. A SPI-MODULE® sputter coater was used for Au-Pd alloy coating under operating conditions of 2 mbar, 15 mA, and 50 s, providing a ~150 Å coating. Operating conditions of FE-SEM were 15 kV accelerating voltage, 5–15 mA current, and 10–20 s counting time for each element. The relationship between particle-size distribution and morphologies was studied with an FEI-Tecnai I 20 transmission electron microscope, operating at 80 kV, using samples dispersed in distilled water and sedimented onto carbon-coated Cu-grids at the University of Georgia, Athens (UGA). Clay slurries were prepared by dilution in distilled water and dispersion in an ultrasonic bath for 10 min. Formvar-covered polymer micro grids were plunged into the clay slurry and dried at room temperature, which provided optimal sample mounting.

Table 2. Chemical composition of the Bodurlar kaolin deposit. Abbreviations: ka: kaolinite, he: hematite.

%	B2-12 ka	B-8 ka	BOD-8 ka	BOD-4 ka	B-7 ka	B2-7 ka+he	B2-13 ka+he	B2-8 ka	B2-17 ka+he	B2-4 ka+he	B2-2 ka
SiO_2	58.33	47.92	50.43	57.27	49.89	55.86	76.90	54.30	57.30	48.13	56.25
Al_2O_3	27.41	36.83	34.68	27.21	35.58	19.78	6.76	31.11	22.40	25.00	30.30
Fe_2O_3	1.96	0.86	0.72	1.58	0.85	12.63	8.18	1.25	7.89	6.77	0.66
MgO	0.19	0.06	0.09	0.46	0.07	0.37	–	0.42	0.50	0.17	0.14
CaO	0.05	0.03	0.02	0.07	0.02	0.05	0.11	0.02	0.07	0.04	0.07
Na_2O	–	–	–	0.10	0.04	0.21	0.08	0.10	0.14	0.06	0.04
K_2O	1.27	1.16	0.43	2.60	0.87	4.40	0.33	3.35	5.15	1.60	0.50
TiO_2	1.03	0.26	0.64	1.68	0.51	0.94	1.32	1.52	1.07	0.59	0.96
P_2O_5	0.28	0.25	0.12	0.18	0.16	0.17	0.88	0.05	0.38	0.54	0.23
LOI	8.82	12.21	12.61	8.35	11.68	4.98	3.72	7.55	4.39	13.54	10.51
Total	99.35	99.59	99.73	99.53	99.67	43.55	21.37	45.38	41.98	48.32	43.40
ppm											
Au	2	–	2.50	–	3	–	–	–	–	1.9	–
As	1.9	8	–	–	4	64	60	–	4	13	7
Ba	971	738	277	783	865	952	687	1064	1354	2054	615
Ce	81	–	91	–	50.9	–	–	–	–	358	–
Cl	–	170	143	477	200	250	93	240	306	148	452
Cu	29	31	18	20	34	163	98	23	115	27	25
Eu	0.6	–	1.7	–	2.3	–	–	–	–	2.8	–
Ga	17	11	12	31	13	23	–	23	22	16	15
Hf	5.2	–	2.8	–	2.4	–	–	–	–	2.9	–
Hg	<0.1	<0.1	<0.1	<0.1	<0.1	<0.1	<0.1	<0.1	<0.1	<0.1	<0.1
La	9	–	23	–	–	–	–	–	–	149.7	–
Mo	0.3	–	–	–	–	–	4	–	8	6	–
Nb	12	10	8	16	6.6	–	15	15	9	7.7	–
Nd	9	–	28	–	–	–	–	–	–	105.9	–
Ni	14	11	–	–	–	–	–	–	–	0.1	13
Pb	39	69	2.3	–	34	–	77	–	46	9.6	–
Rb	43	32	16	96	25	106	–	118	96	28	14
S	1548	683	588	815	735	–	1415	459	379	1488	–
Sc	–	–	–	–	–	42	–	–	–	46	–
Sr	744	640	318	472	280	38	1395	48	643	627	361
Ta	–	–	0.5	–	0.5	–	–	–	–	0.5	–
Th	–	–	5.4	–	4.9	–	–	–	–	8.1	–
Y	20	160	13	56	69	40	–	38	–	12.8	–
Zn	38	25	17	34	–	25	42	18	37	21	17
Zr	331	167	115	299	100	183	314	301	191	169	176

https://doi.org/10.1346/CCMN.2016.0640305 Published online by Cambridge University Press

Table 3. Sulfur isotopic composition of alunite samples.

Sample ID	$\delta^{34}S$ (‰)
SA1-t	1.7
SA2-10	3.6
SA2-15	3.0
SA2-19	3.8
SA3	3.1
SIG2-2	4.1
SIG2-4	2.7
SIG3-3	2.4
SIG3-4	2.4
SIG4-10	3.6

Nine alunite samples were analyzed at UGA for sulfur isotopes (Table 3). Gaseous SO_2 was produced by heating alunite at 1050ºC and analyzed by a Finnigan MAT 252 gas-source mass spectrometer. The $\delta^{34}S$ values are reported relative to the primary standard, Vienna Canon Diablo Troilite (VCDT). The accuracy was estimated to be ±0.2‰. The $\delta^{18}O$ and δD analyses for kaolinite were made on the Finnigan MAT 252 or Finnigan Delta E spectrometer at the UGA. Gases were extracted using laser ablation and heating for the $\delta^{18}O$ and δD, respectively (Table 4).

$^{40}Ar/^{39}Ar$ step-heating for mineral age determination was carried out on four alunite samples taken from the Sarıbeyli-Sığırlı deposits (Table 5). All samples were taken from currently operating kaolin quarries and near the fault zones, and were considered to represent advanced argillic alteration. $^{40}Ar/^{39}Ar$ age determinations were made at the University of Michigan. Samples were analyzed by the furnace step-heating method using a double vacuum resistance furnace similar to the Staudacher *et al*. (1978) design. Details of the analytical methods and data treatment are given in Justet and Spell (2001) and Spell and McDougall (2003).

Fourier-transform infrared (FTIR) analysis was performed on a Perkin Elmer Spectrum 100 FTIR spectrophotometer at ITU using KBr pellets (13 mm) at a concentration of 1%. Spectra were recorded in transmission mode immediately after pellet preparation; the scanning range was 400−4000 cm^{-1}, with a resolution of 4 cm^{-1}, and five scans signal-averaged for each sample. A Renishaw in Via® Raman spectrometer equipped with a Leica RE02® microscope was used for spectral data collection. Laser excitation sources of λ = 442 and 785 nm were used. The instrument was calibrated using a silicon standard at 520.5 cm^{-1}. The Raman analysis was restricted to an area less than 2 mm in diameter. The laser power was reduced using neutral-density filters and was typically between 1 mW and 220 mW at the sample. Spectra were recorded over the range 100 to 4000 cm^{-1} using an integration time of 2 h and smoothed using a seven-point running average. Resolution on channel wavelength was less than 0.1 cm^{-1}.

Differential thermal analysis, differential scanning calorimetry (DSC), and differential thermogravimetric (TGA) analyses were performed using a TA Instruments SDT Q600 thermal analysis system. Initial heating was set at 30ºC with a heating rate of 10ºC/min up to 900ºC in an argon atmosphere (the rate varied when weight loss occurred and the weight stabilized).

RESULTS

Sarıbeyli-Sığırlı deposit

Four quarries are present in this deposit within the same micro graben (Figure 2). Petrography of unaltered

Table 4. O and D isotopic composition of kaolinite samples and calculated formation temperature, assuming that the $\delta^{18}O$ value of meteoric water is −4.5‰ (value taken from Ece *et al*., 2013).

Sample ID	$\delta^{18}O$ (‰)	δD (‰)	Model formation temperature (ºC)
Sarıbeyli-Sığırlı			
SA2-22	10.9	−70	79
SA2-26	6.7	−97	118
SA2-27	–	−61	–
SA4	12.6	−89	66
SIG2-3	7.9	−53	106
SIG2-5K	8.6	−83	100
SIG2-6	9.2	−84	94
SIG3-2	11.0	−84	79
SIG3-6	10.7	−92	85
Bodurlar			
B7	17.0	−99	39
B8	16.7	−93	40
BOD-4	14.5	−90	54
BOD-8	15.0	−94	50

https://doi.org/10.1346/CCMN.2016.0640305 Published online by Cambridge University Press

Table 5. Age analyses of magmatic and altered rocks in the study area.

Area	Rock	Rock/mineral	Age	Reference
Kirazlı	Basalt	Whole rock	31.1 ± 0.7 27.6 ± 0.6	Ercan *et al*., 1995
	Andesite	Whole rock	24.8 ± 1.2	Ercan *et al*., 1995
	Altered rock	Alunite	30.7 ± 1.5	Yiğit, 2012
	Argillic-phyllite Zone	Whole rock	24.7 ± 1.2 26.3 ± 1.3	Ağdemir *et al*., 1994
Kuşçayırı	Granodiorite	Hornblende	35.7 ± 0.8 39.4 ± 0.8	Delaloye and Bingöl, 2000
	Altered rock	Alunite	39.4 ± 0.6	Yiğit, 2012
Kartaldağ	Dacite porphyry	Biotite	42.2 ± 0.5	Ünal, 2010
	Granodiorite	Hornblende	40.8 ± 0.5	
	Altered rock	Alunite	38.8 ± 1.1	Yiğit, 2012
Ağıdağı	Altered rock	Alunite	26.4 ± 0.9	Yiğit, 2012
Alanköy	Granodiorite	Hornblende	28.3 ± 2.6	Yiğit, 2012
			27.9 ± 0.2	
	Altered rock	Alunite	30.7 ± 1.5	Ağdemir *et al*., 1994
			13.6 ± 1.7	
Sarıbeyli-Sığırlı	Altered rock	Alunite	34.2 ± 0.2 33.2 ± 0.18 32.5 ± 0.18 32.7 ± 0.17	This study

host volcanics near the Sarıbeyli-Sığırlı deposit revealed very thin (sub-millimeter) zonations on the outer periphery of clinopyroxene grains, which suggests that the magma was not in total equilibrium at the time of cooling. The andesites consist mainly of euhedral zoned and polysynthetic twinned plagioclase and clinopyroxene phenocrysts. Biotite and amphibole are less abundant than plagioclase and pyroxene, but when present they appear more affected by hydrothermal alteration evidenced by sericitization and oxidized phases seen in thin-section. The matrix of unaltered rocks consists of plagioclase microlites, very fine-grained crystals, and glasses. The tuffs are generally massive but exhibit changes in particle size from blocky to lapilli tuffs to ash tuffs over short distances (<1 m). Most glass shards in the tuffs become devitrified following the hydrothermal alteration processes. Massive andesitic tuffs consist mainly of plagioclase and biotite.

Alteration of varying degrees appears at the quarry site (Figure 2), with reaction zone haloes reaching thicknesses of up to 60 m for Sa1, 20 m for Sa2 and Sa4, and 6 m for Sa3. XRD analyses showed that alteration mineral assemblages comprise kaolinite, α-quartz, alunite, dickite, minor illite, and boehmite or diaspore. Kaolinite occurs with a range of order, having Hinckley indices from 1.33 to 0.8 (Hinckley, 1963), which likely represents a mixture of high- and low-defect kaolinite (Plancon *et al*., 1988) and some halloysite, which was only seen in SEM. Dickite occurs displaying a well ordered structure (SA2-22 in Figure 4). Kaolinite and dickite were distinguished with XRD using their distinctive high angle reflections at 1.34, 1.307, and 1.284 Å and at 1.337, 1.316, and 1.283Å, respectively (Moore and Reynolds, 1989 – table 7.6; Zotov *et al*., 1998). Some samples contained mixtures of dickite and kaolinite (*e.g.* see SA2-26 in Figure 5).

Both FTIR and Raman spectroscopy have the potential to distinguish dickite from kaolinite and halloysite. The IR bands for the hydroxyl-stretching band region showed the bands of dickite at 3699, 3652, and 3621 cm^{-1} (Figure 6). The IR bands of kaolinite appeared at 3696, 3670, 3652, and 3620 cm^{-1}. These results are similar to the findings of OH-stretching modes of Ehrenberg *et al*. (1993) and Balan *et al*. (2010). Mixtures of dickite and kaolinite have averaged strongest intensity forming bands of medium-strong intensity, for example at ~3620 cm^{-1}. Between these bands the absorption (at ~3652 cm^{-1}) was relatively weak. Brindley *et al*. (1986) showed that interlayer hydrogen bonding is weaker in dickite than in kaolinite and the frequency of the v_1 stretching band of the inner-surface hydroxyls increases sequentially from well-ordered kaolinite through the disordered structures to well-ordered dickite (see also Joswig and Drits, 1986; Frost, 1995; Balan *et al*., 2014).

Raman spectroscopy produced results that varied with excitation wavelength, crystal orientation, and temperature. Each of these factors has been shown to affect band frequency and intensity of active modes

https://doi.org/10.1346/CCMN.2016.0640305 Published online by Cambridge University Press

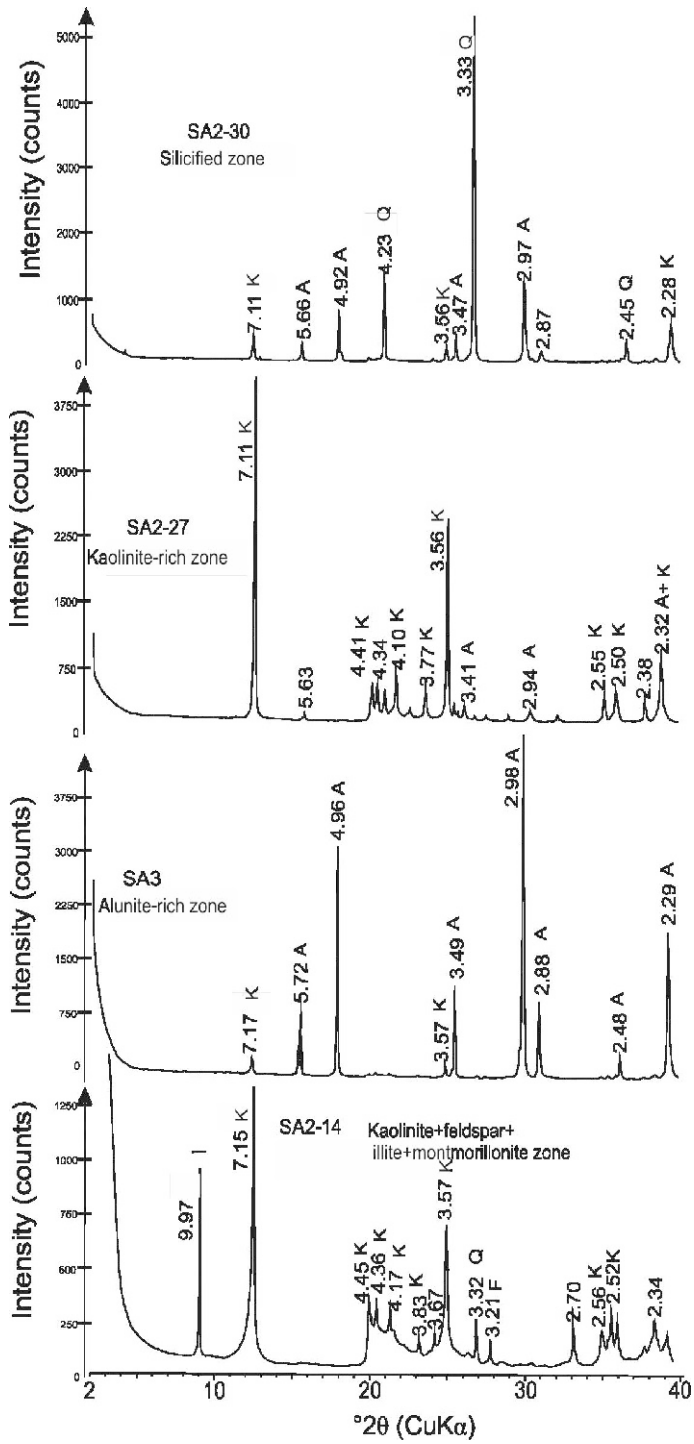

Figure 4. XRD patterns for rock samples from the Sarıbeyli-Sığırlı deposit using CuKα radiation. Minerals identified include quartz (Q), kaolinite (K), and alunite (A). Patterns are representative of (1) Silicified zone. SA2-30 is along the fault and it is α-quartz-rich; (2) Kaolinite-rich zone. SA2-27 is from the <2 μm size fraction and is several meters from the fault zone; (3) Alunite-rich (A) zone, SA-3 is taken 2 m from fault zone; and (4) weathered zone. SA2-14 is ~10 m from the fault zones and contains feldspar and illite.

(Johnston *et al*., 1998; Frost *et al*., 2001). Spectra were collected using laser wavelengths (λ) of 785 nm and 442 nm, which only produced three of five absorption peaks (ν_{1a}, ν_2, and ν_5, respectively) that correspond to kaolinite and dickite O-H bands. Previous studies (Frost, 1995; Johnston *et al*., 1998; Frost *et al*., 2001) used

https://doi.org/10.1346/CCMN.2016.0640305 Published online by Cambridge University Press

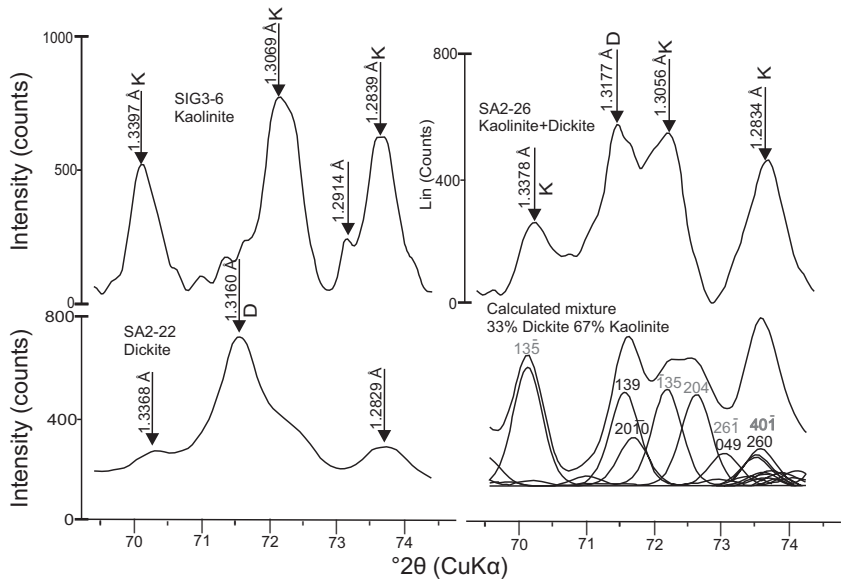

Figure 5. Kaolinite and dickite XRD patterns from 69.5 to 74.5°2θ obtained using CuKα radiation. Patterns are for SIG 3-6 kaolinite (< 2 μm), SA2-22 dickite (< 2 μm), SA2-26 kaolinite+dickite (<2 μm), and a modeled pattern using a 2:1 mixture of kaolinite:dickite. The model parameters included a coherent scattering domain size of 18 nm from the *CrystalDiffrac*® software. Major *hkl* reflections are noted for each phase. Dickite (black) and Kaolinite (gray).

excitation wavelengths greater and lower than 785 nm (*i.e.* λ =1064, 633, 514, and 325 nm). In the present study, no differences were observed among data sets using λ = 785 nm (data not shown); however, differences were observed at λ = 442 nm (Figure 7). Direct comparisons between this data set and others published (Frost, 1995; Frost *et al*., 2001) using different λ conditions were tenuous; however, a general observation is that the ratio of the band intensities of ν_1:ν_5 for kaolinite *versus* dickite are consistently higher for kaolinite. The ν_1:ν_5 intensity ratio for sample from SIG3-6 was much higher than SA2-22 (Figure 7), which suggests that the two samples are composed predominantly of kaolinite and dickite, respectively.

Morphology characterized through the FE-SEM studies revealed two dominant habits of kaolin polymorphs found in association with partially dissolved feldspars (Figure 8a). One habit appeared as randomly oriented crystals with dimensions between 500−2000 nm (Figure 8b). The other habit of kaolinite was book-like stacks of platelets with dimensions between 1000−2000 nm (Figure 8c). Coexisting pseudo-hexagonal alunite crystals ranged from 3000 to 9000 nm (Figure 8d) and show signs of dissolution at the surface as small pits (Figure 8f). Kaolinite was occasionally found as equi-dimensional crystals (Figure 8e). Dickite with its characteristically blocky habit was not observed with FE-SEM. In this study,

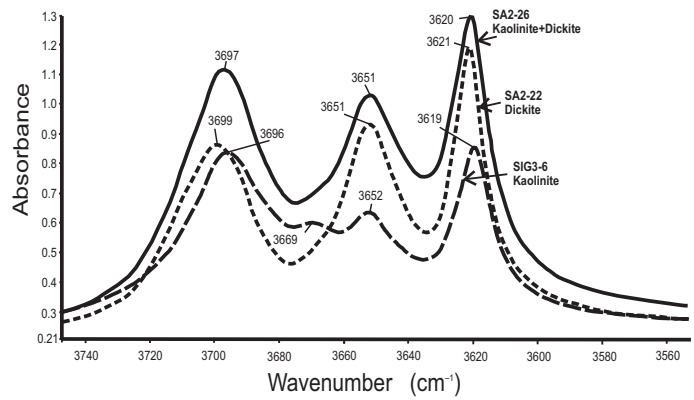

Figure 6. Absorption spectra of the IR-active, fundamental O−H stretch region, which helps to distinguish kaolinite from dickite and mixtures of kaolinite and dickite samples (SIG3-6, SA2-22 and SA2-26, respectively). The vertical scale is relative absorbance.

https://doi.org/10.1346/CCMN.2016.0640305 Published online by Cambridge University Press

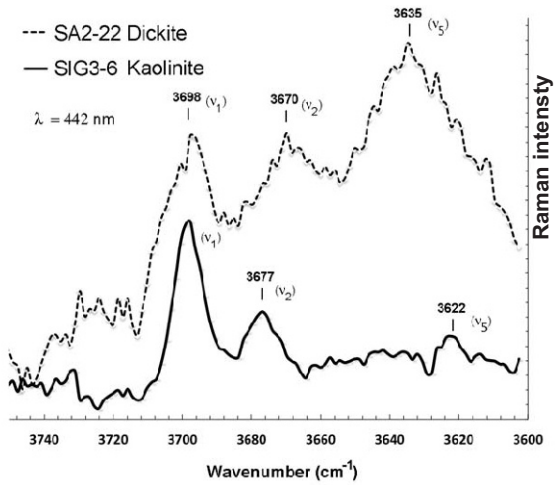

Figure 7. Raman spectroscopy distinguishes kaolinite (SIG 3-6) and dickite (SA2-22) by relative intensity of the active modes. The ratio of ν_{1a} to ν_5 is greater for kaolinite. The excitation wavelength was 442 nm.

dickite did not appear to take this blocky form. Alunite crystals from the Sarıbeyli-Sığırlı deposit are about 3000−6000 nm in size (Figure 8g). Halloysite appeared as a minor phase showing open-ended tubular morphology with internal lumen diameters of 10−20 nm and outer diameters of 45−200 nm (Figure 8h). Anhedral 500 nm quartz crystals were often scattered on the other mineral surfaces. The FE-SEM observation showed alunite was always associated with halloysite.

TEM revealed halloysite that displayed a tubular habit with a lumen interior (Figure 9a). The electron density contrast clearly displayed ~400−500 nm long and continuous hollow tubes with open ends (Figure 9a and 9b). Growing halloysite tubes were also observed at the edge of pseudo-hexagonal particles of kaolinite (Figure 9b). The outer and inner diameters of these long tubes averaged ~100 nm and ~30 nm, respectively (Figure 9a). The TEM revealed possible dickite, mainly in the shape of unusually large particles >2 mm wide (Figure 9e). Kaolinite platelets were generally <1.5 mm in diameter (Figure 9b,c,d,f); however, ultra-fine particles of kaolinite ~15 nm in diameter occasionally appeared (Figure 9d), along with other coarse particles of kaolinite covered with small silica spheres.

The DTA peaks of dickite and kaolinite from the Sarıbeyli-Sığırlı kaolin deposit recorded different endotherm temperatures (Figure 10), even though each produced ~1 wt.% loss at 50ºC, 12.4 wt.% loss above 550ºC, and an additional 1 wt.% loss above 700ºC. Samples dominated by vermiform booklet stacks of kaolin platelets exhibited an asymmetrical endotherm peak at 575ºC. Samples dominated by dickite had an endotherm peak at 658ºC, which also exhibited a slightly sharper peak (Brindley and Porter, 1978). Both kaolinite and dickite lost about 14% of their mass by ~696ºC, suggesting complete dehydroxylation. The 1 wt.% loss observed above 700ºC may be attributed to small amounts of alunite, as noted by Ece and Schroeder (2007).

Bodurlar deposit

The Bodurlar deposit occurs in the Oligocene volcanic rocks dominated by andesitic lavas and tuffs (Figure 3). The Bodurlar kaolin deposit covered an area approximately 2 km^2 with six fracture zones, which are filled with quartz and silicified rocks. Hydrothermal alterations developed on both sides of these fracture zones (Figure 3). White and massive deposits of kaolin and quartz included various iron (oxyhydr)oxides.

XRD analysis indicated the common minerals were kaolinite, α-quartz, halloysite, alunite, minor illite, and sparingly abundant montmorillonite (Figure 11). The Bodurlar deposit consisted of high abundances of kaolinite and quartz, and low amounts of alunite, jarosite, and halloysite. Alunite and jarosite increased in abundance where the alteration was more intense. Very fine-grained quartz filled the six fault zones in the middle of the kaolin quarry (Figure 3) and, in some places, distinct vuggy residual quartz was present. Pores of the vuggy quartz were filled with iron (oxyhydr)-oxides (hematite and goethite) and pervasive silicification was found throughout the deposit.

Morphological characterization of the Bodurlar samples using the FE-SEM revealed silica coating of surfaces (Figure 12a) and kaolinitization of feldspars (Figure 12b). The Bodurlar samples showed excellent examples of halloysite tubular structures undergoing transformation to kaolinite (Figure 12c−h). This transformation was clearly shown as serration-like crystal habit on halloysite tubes (Figure 12e,f). Halloysite appeared with hollow open-ended tubular morphology, having internal lumen diameters of 10−20 nm and outer diameters of 110−220 nm (Figure 12f,g,h). Hillier *et al*. (2016) explained that the relationships between geometric form and size characteristics suggest that the prismatic morphology is formed as a natural consequence of continued tube growth rather than as a result of dehydration. Some kaolinite crystals occurred as curved flakes with dimensions between 2000−4000 nm (Figure 12d). Two types of kaolinite were observed in the SEM studies: (1) equidimensional,

Figure 8 (*facing page*). FE-SEM images of minerals from the Sarıbeyli-Sığırlı deposit listed by sample number and deposit: (a) feldspar crystals with kaolinite occurrences (SA2-22; Sa1); (b) randomly oriented kaolinite crystals (SIG2-5K; Sa2); (c) vermiform (book-shaped) kaolinite crystals (SIG2-5K; Sa2); (d) euhedral alunite crystals (SIG4-12; Sa4); (e) hexagonal equidimensional kaolinite (SIG2-5K; Sa2); (f) alunite dissolution pits (SA2-10; Sa1); (g) alunite crystals (SIG4-10; Sa4); and (h) tubular-shaped halloysite showing a hollow lumen (SA2-12; Sa1).

https://doi.org/10.1346/CCMN.2016.0640305 Published online by Cambridge University Press

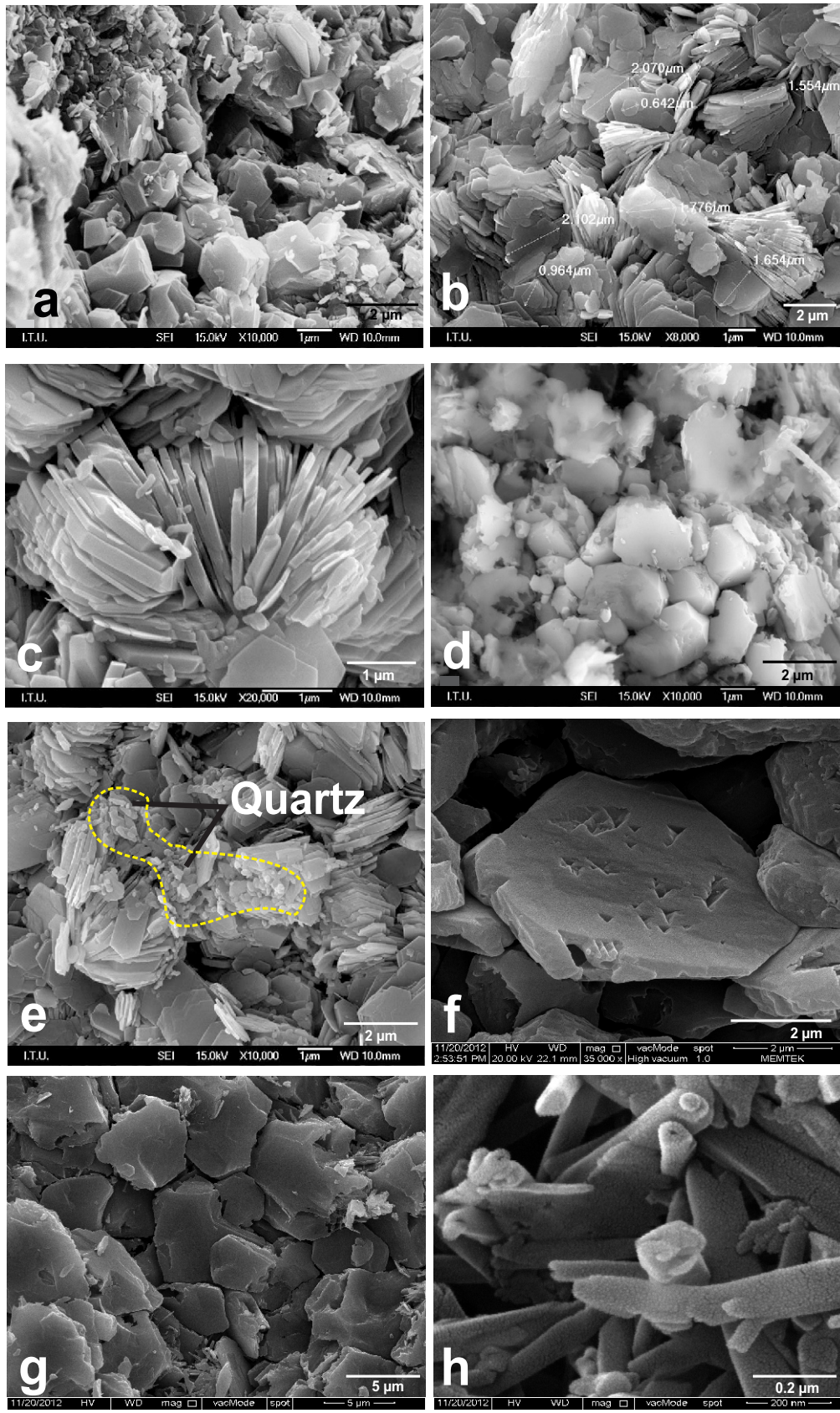

https://doi.org/10.1346/CCMN.2016.0640305 Published online by Cambridge University Press

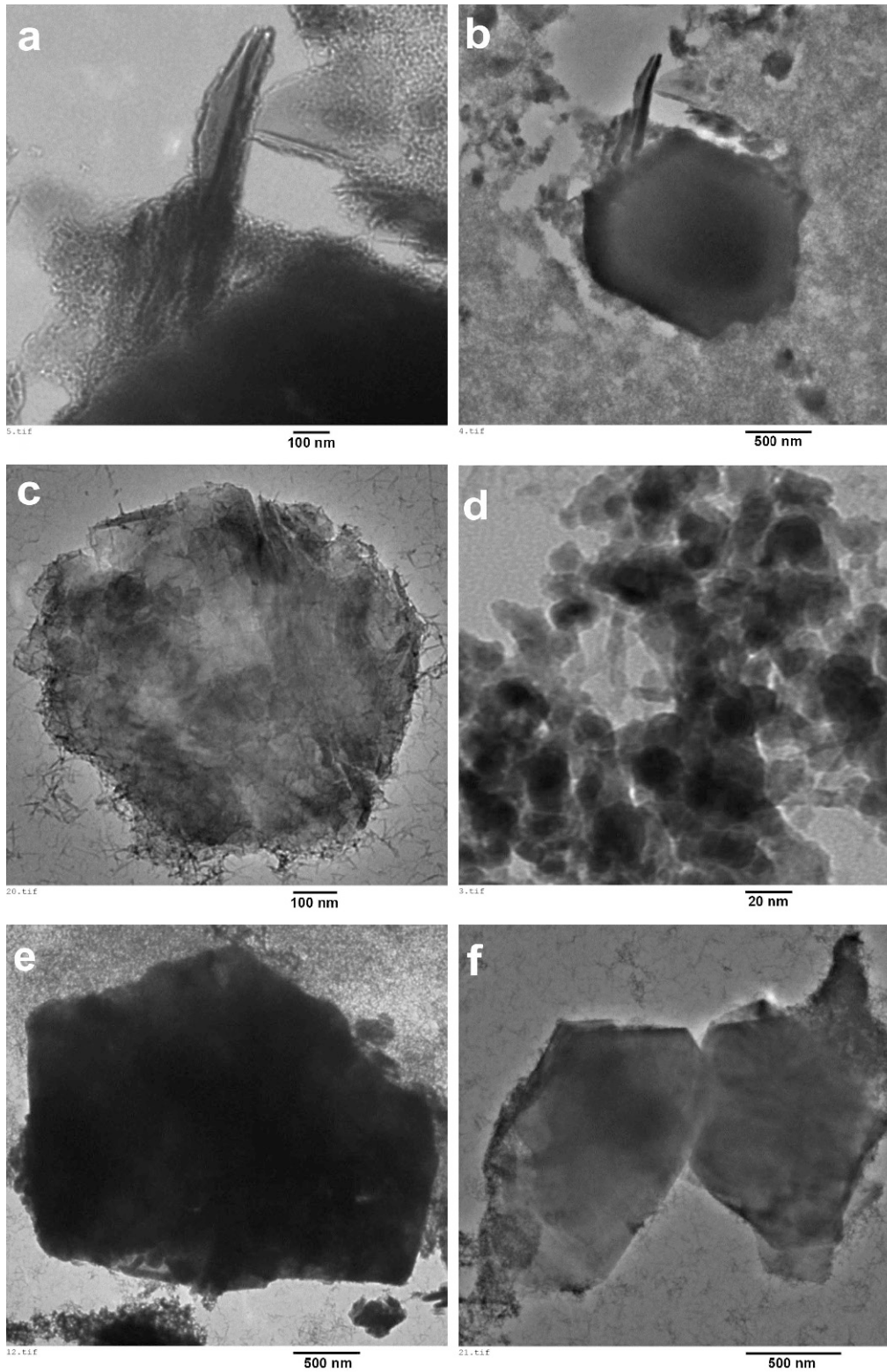

Figure 9. TEM images of kaolins show the morphology of halloysite, kaolinite, and dickite crystal habits. (a) Halloysite tubes with electron-dense areas along the curls of tube axes in (SIG-4-10); (b) pseudohexagonal kaolinite particles with smooth surfaces and tubular halloysite at the edge (SIG-4-10); (c) kaolinite formed from alteration of a mica fragment (SIG-3-6); (d) ultra-fine particles of kaolinite covered with small silica spherules (SIG-3-6); (e) thick dickite crystal with well defined outline and smooth surface (SA2-22); (f) kaolinite crystal with step-like growth features (SIG-3-6).

https://doi.org/10.1346/CCMN.2016.0640305 Published online by Cambridge University Press

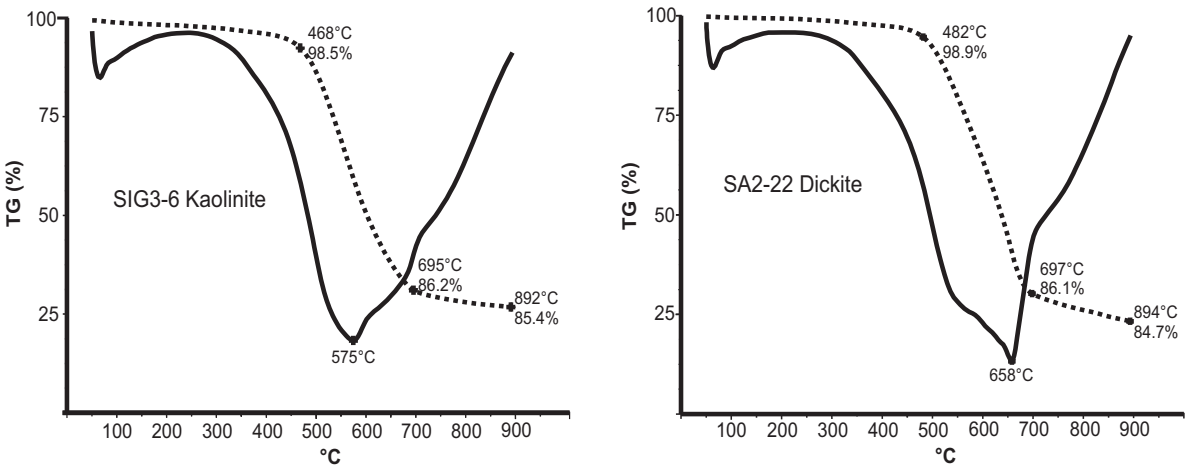

Figure 10. DTA/TG curves of SIG 3-6 kaolinite and SA2-22 dickite samples. Both produce a ~1 wt.% loss at 50ºC, 12.4% loss above 550ºC, and another 1 wt.% loss above 700ºC. The notable difference is the higher peak endotherm of dickite when compared to kaolinite. Inflection values are 658ºC and 575ºC for dickite and kaolinite, respectively.

<1000 nm, and (2) coarser-grained with dimensions of 2000−4000 nm. Figure 13 shows a schematic representation of the various crystal habits.

Stable isotope geochemistry

The $\delta^{34}S$ isotopic values (Table 3) ranged from +1.7 to +4.1‰ in the Sarıbeyli-Sığırlı kaolinites and reflect

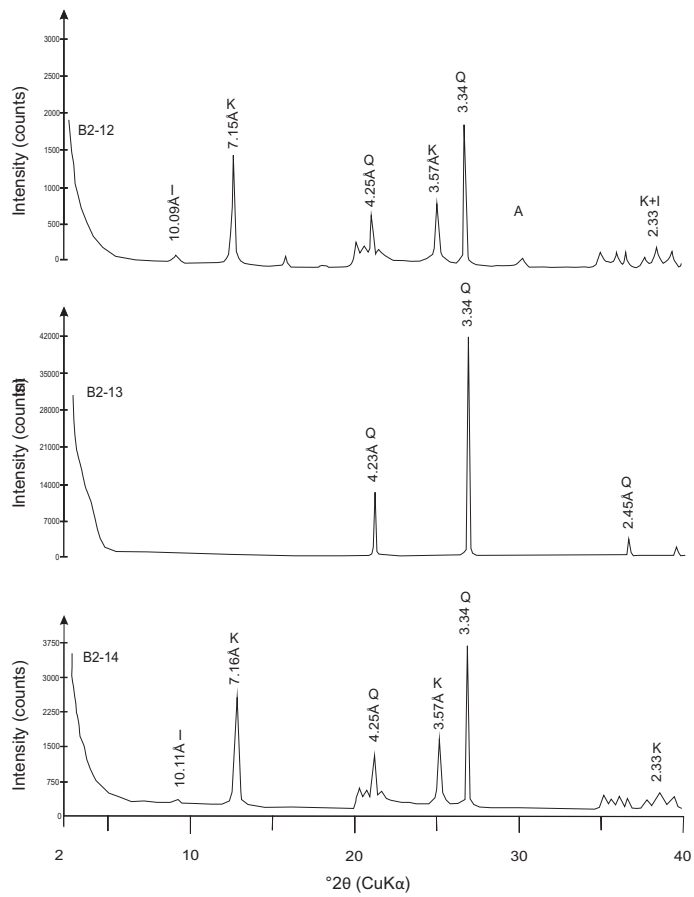

Figure 11. XRD patterns of the Bodurlar deposit whole-rock samples. Pattern for B2-12 shows an assemblage of mica, kaolin group, alunite, and quartz. B2-13 presents α-quartz taken from the fault zone. B2-14 shows an assemblage of mica, a kaolin-group mineral, and quartz.

https://doi.org/10.1346/CCMN.2016.0640305 Published online by Cambridge University Press

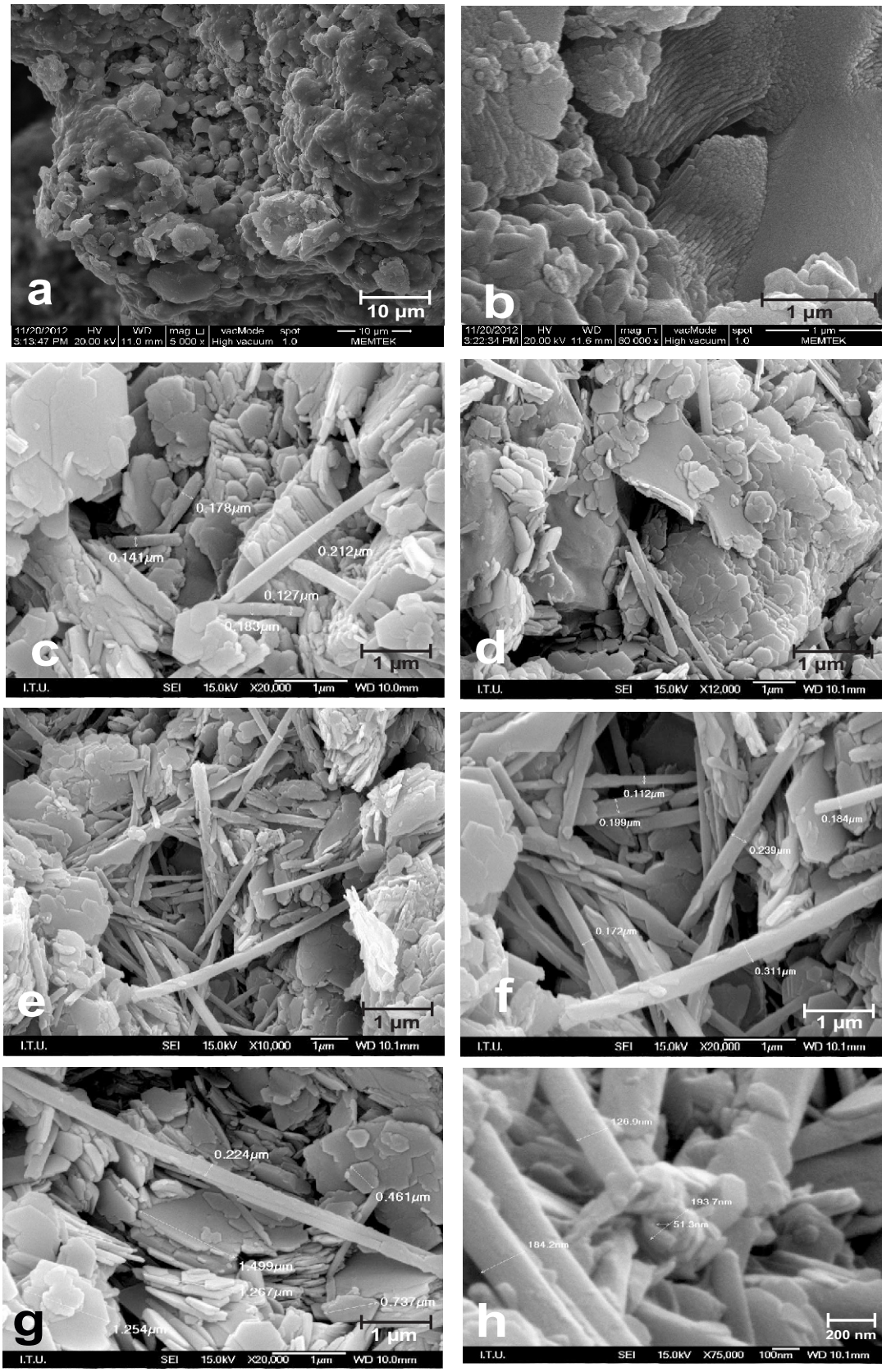

https://doi.org/10.1346/CCMN.2016.0640305 Published online by Cambridge University Press

formation from a magmatic-hydrothermal derived sulfur source (−3/+3‰; Rye *et al*., 1992). Alunite was not sufficiently abundant in the Bodurlar deposit to allow for $\delta^{34}S$ isotopic analysis. $\delta^{18}O$ and δD values of kaolins from both deposits are shown in Table 4. The $\delta^{18}O$ isotopic values of the Sarıbeyli-Sığırlı kaolinites ranged from +6.7‰ to +12.7‰ and δD values ranged from −61‰ to −97‰. The isotopic values of the Bodurlar kaolins ranged between +14.5‰ to +17‰ for $\delta^{18}O$ and −90‰ to −99‰ for δD.

$\delta^{18}O$ and δD values from the Sarıbeyli-Sığırlı deposit cluster on a plot (Figure 14) that has a lower $\delta^{18}O$ value and a more enriched δD‰ value compared to those from the Bodurlar deposit. When comparing model equilibrium lines for kaolinite and halloysite at different temperature in the range of 20º to 100ºC and to the supergene/hypogene (S/H) line of Sheppard and Gilg (1996) in Figure 14, the values indicate that Sarıbeyli-Sığırlı kaolins formed at a higher temperature (and possibly under the influence of magmatic water). If, however, both deposits were assumed to have formed from waters with the same $\delta^{18}O$ and δD compositions and rock/water ratios, then it is possible to calculate the formation temperature of kaolinites using the isotopic fractionation factor equation of Sheppard and Gilg (1996) (also assuming meteoric water $\delta^{18}O = -4.5‰$ for the Oligocene; this value is taken from Ece *et al.*, 2013). Formation temperatures of the Sarıbeyli-Sığırlı deposit ranged from 66ºC to 118ºC and formation temperatures of the Bodurlar deposit ranged from 40ºC to 54ºC (Table 4).

Geochronology

Four nearly pure alunite samples from the Sarıbeyli-Sığırlı deposits were selected for $^{40}Ar/^{39}Ar$ age dating (Figure 15). Model ages were calculated to be 32.5 ± 0.2, 32.7 ± 0.2, 33.2 ± 0.2, and 34.2 ± 0.2 Ma (Table 5). The Kuşçayırı granitic intrusion is proximal to the Sarıbeyli-Sığırlı deposits and the granite mineralization is slightly older than alunite (Table 5). The Camyayla granitic intrusion with 35.7 ± 0.8 and 39.4 ± 0.2 Ma hornblende age (Söylemezoğlu, 2010) is very close to the Bodurlar deposit and hydrothermal alteration, and is proposed here to be related to a granite replacement process.

Radiometric ages for volcanics of the Biga Peninsula have been studied extensively using mainly unaltered rocks (Fytikas *et al*., 1976; Altunkaynak and Genç, 2008; Altunkaynak *et al*., 2012a). Table 5 and Figure 16 show all known $^{40}Ar/^{39}Ar$ ages from the region where both primary volcanic minerals and secondary alteration minerals where examined. Ages of volcanic rocks in the vicinity of nearby Kirazlı (east of study area) ranged from 31.1 to 24.8 Ma, whereas the age of alunite samples from the altered rocks ranged from 30.7 to 26.3 Ma. Hornblende ages of the Kuşçayırı granodiorite, also close to the study area, ranged from 39.4 to 35.7 Ma, and the age of alunite in related altered rocks is 39.4 Ma. Similar age relations were observed between the Kartaldağ and Alanköy granodiorites and the alunite samples in the surrounding altered rocks (Table 5).

DISCUSSION

Sarıbeyli-Sığırlı zonation

Alteration of the Sarıbeyli-Sığırlı (S) deposit exhibits lateral zonation that can be divided into mineral assemblages that vary gradually away from the fault zones. These four assemblages were as follows: Zone S-*i* (silicified) → Zone S-*ii* (alunite) → Zone S-*iii* (kaolinite-hydrothermal), and Zone S-*iv* (kaolinite-less altered).

Zone S-*i* contained (in order of abundance) quartz ± alunite ± kaolinite/dickite/halloysite. All quarries of the Sarıbeyli-Sığırlı deposit have zone S-*i* in three distinct silicified settings. The first was within fault zones, the second was in silica cap rocks, and the third was a pervasive silicification of tuffs. Silica-filled fault zones were 10 to 50 m wide and about 2000 m in length. Within the F1 and F2 faults, the silicified zone was 5−10 m wide and ~750 m long (Figure 2). Massive gray silica caps occurred along the southern borders of F1. Silicified rocks were observed near the fault zones, where quartz was accompanied by a significant amount of alunite, dickite, and kaolinite minerals. Hematite and other Fe (oxyhydr)oxide minerals also occurred in silicified altered rocks. Based on field observations, silicified tuffs and quartz-filled fault zones were exposed in the Sa2, Sa3, and Sa4 quarries, whereas they were not observed in Sa1. The Sa4 quarry was the most silicified. Silicified tuffs were characterized by having higher contents of As (up to 187 ppm), low Hg (up to 0.89 ppm), and high Ba (384−7060 ppm) (Table 1).

Zone S-*ii* contained (in order of abundance) alunite + kaolinite/dickite/halloysite ± quartz. This mineral assemblage was just outside the silicified zone, where alunite occurred earthy or yellowish in color. Alunite was always associated with kaolinite and quartz minerals in varying percentages, but was also found as nearly pure alunite zones, which extended for a few meters (1−2 m). Halloysite was not detected in XRD analyses, but was observed in FE-SEM analysis (Figure 8h). Dissolution

Figure 12 (*facing page*). FE-SEM images of kaolinites, quartz, and halloysite from the Bodurlar deposit: (a) euhedral quartz crystals; (b) botryoidal quartz after lepispheres; (c) well and poorly formed kaolinites; (d) curling kaolinite crystals; (e) irregularly distributed intersection of tubes shown as thin needle-shaped halloysite tubes; (f) halloysite crystals exhibit psuedohexagonal forms on the edges of curls; (g) curling kaolinite crystals range from 460 to ~1500 nm wide; and (h) outside diameters of halloysite tubes range from 126 to 193 nm and the inside diameter is ~50 nm; the halloysite tubes also exhibit an onion skin-type layer morphology.

https://doi.org/10.1346/CCMN.2016.0640305 Published online by Cambridge University Press

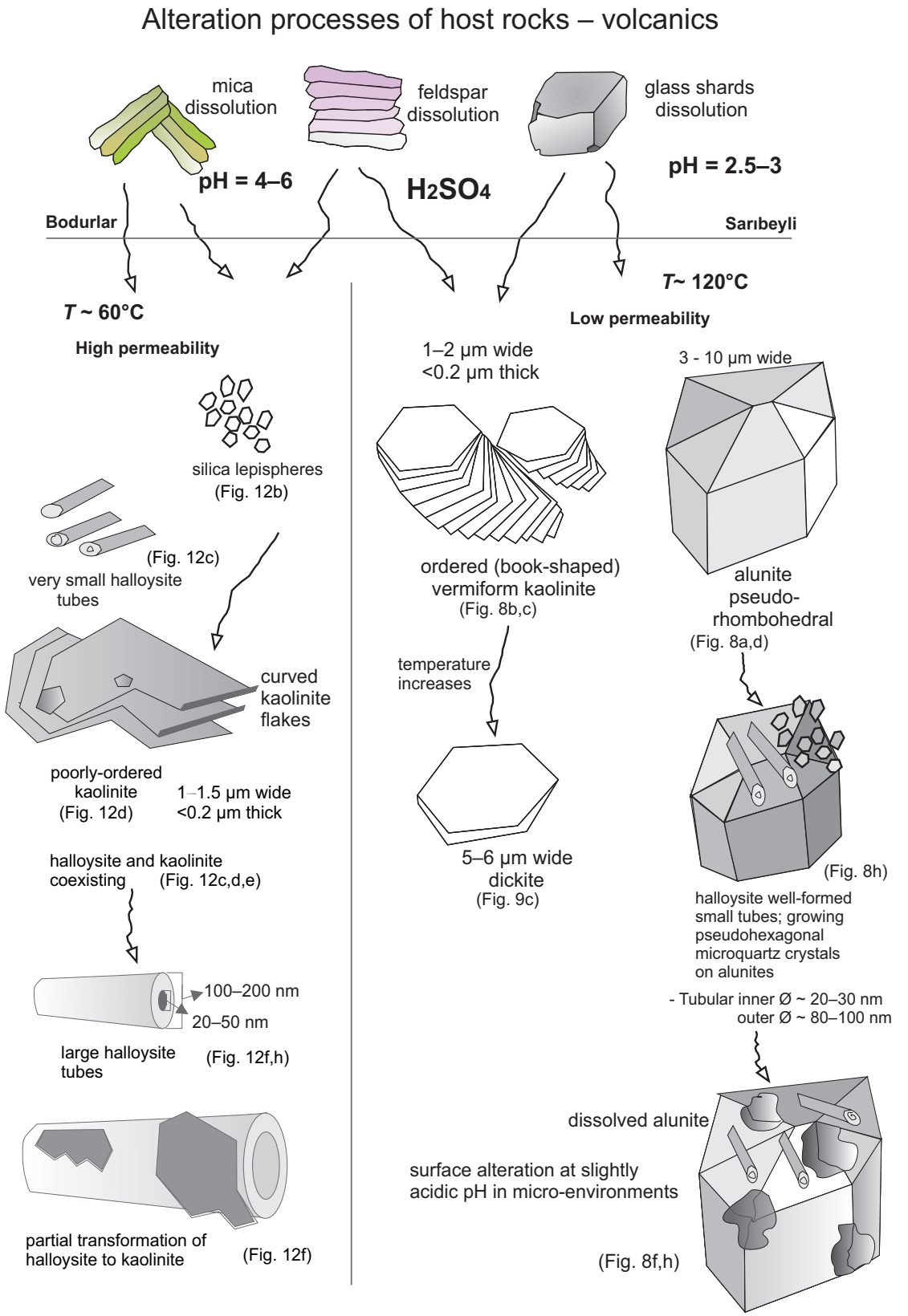

Figure 13. The summary of hydrothermal alteration and dissolution processes of andesitic tuffs to kaolinite and alunite – summarized according to FE-SEM studies (modified from Ece *et al.*, 2013).

https://doi.org/10.1346/CCMN.2016.0640305 Published online by Cambridge University Press

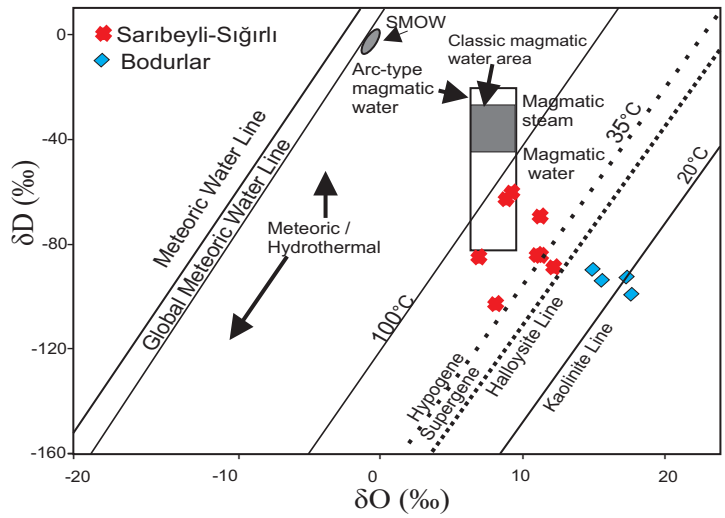

Figure 14. The $\delta^{18}O$ and δD values of kaolins from the Sarıbeyli-Sığırlı and Bodurlar deposits, hydrothermal kaolins from active geothermal fields, and thermal waters near kaolin locations in Japan (Hayba *et al*., 1985). The meteoric water line is $\delta D = 6.8\ \delta^{18}O + 10.5$ (Harris *et al*., 1999). Supergene *vs.* hypogene (S/H) lines are taken from Sheppard and Gilg (1996). Equilibrium lines for kaolinite and halloysite at various temperatures were calculated assuming meteoric water $\delta^{18}O = -4.5‰$ for the Simav region during the Oligocene period (Ece *et al*., 2013).

pits were observed on the alunite surfaces, which can be interpreted to be either a result of secondary surface weathering or dissolution under highly acid conditions (Figure 8f). Halloysite occurs with alunite and probably forms under acidic conditions. Alunite abundances varied within the alteration zones. For instance, Sa1 and Sa4 deposits were more alunite-rich than Sa2 and Sa3 deposits, as evidenced by the higher Al_2O_3 (up to 44.51 wt.% in SA2-10; Table 1) and low SiO_2 (down to 5.74 wt.%). The theoretical maximum Al_2O_3 content of alunite is 36.92 wt.%. Higher values indicate the presence of small amounts of gibbsite or boehmite as weathering products of kaolin in very small areas close to the surface. Although neither gibbsite nor boehmite was observed by XRD in this study, they have been reported in surrounding deposits near the study area (Hatipoglu *et al*. 2010). Notably, this zone has high As (up to 202.8 ppm), Sb (126.3 ppm), and Ba (1380 ppm) concentrations (Table 1).

Zone S-*iii* contains (in order of abundance) kaolinite ± alunite ± quartz. This alteration zone represented the economic part of the deposits. This massive and white kaolinite deposit extended 60 m vertically and 400 m laterally at the Sa1 mine. Zonal extents were smaller in the other mines with vertical and lateral dimensions of 20 m × 200 m, 5 m × 100 m, and 20 m × 50 m for Sa2, Sa3, and Sa4 mines, respectively. XRD analyses indicated that some samples contain up to 100 wt.% kaolin group minerals. Very few samples in this alteration zone contain dickite. This part of the deposit most typically has up to 50 wt.% kaolin group minerals and up to 50 wt.% alunite with lesser amounts of quartz. Kaolin group-rich samples contain the highest Al_2O_3 (up to 48 wt.%), and low Na_2O, Ca_2O, and K_2O (Table 1). These high Al_2O_3 values in kaolin suggest the presence of boehmite, diaspore, or gibbsite in "*advanced argillic*" alteration zones, as mentioned above. These samples contained high Pb (up to 779 ppm), S (up to 8632 ppm), V (up to 757 ppm), and As (up to 169 ppm).

Zone S-*iv* contained (in order of abundance) kaolinite + feldspar + illite ± montmorillonite. This assemblage occurred away from fault zones and some the original texture of tuffs was destroyed due to lower intensity chemical reactions of acidic geothermal and meteoric waters. Relict rock textures and K-feldspars were observed in the thin sections of tuffs.

Bodurlar zonation

Common alteration minerals in the Bodurlar (B) deposit were kaolinite, α-quartz, halloysite, alunite, and jarosite, with minor amounts of illite and even lesser amounts of montmorillonite (Figure 11). Very fine-grained quartz minerals filled the six fault zones passing through the quarry (Figure 12a, b) and, in some places, distinct residual quartz with vuggy textures was found. Pores were filled with iron (oxyhydr)oxide minerals (*e.g.* hematite, goethite). Mineral assemblages changed away from the fault zones in three assemblages B-*i* (silicified) → B-*ii* (kaolinite-hydrothermal) → B-*iii* (kaolinite-less altered) and were as follows.

Zone B-*i* contained (in order of abundance) quartz ± kaolinite ± alunite ± jarosite. Silicified zones (Figure 3) were formed likely by precipitation from geothermal waters. These fluids were inferred to be silica-rich

https://doi.org/10.1346/CCMN.2016.0640305 Published online by Cambridge University Press

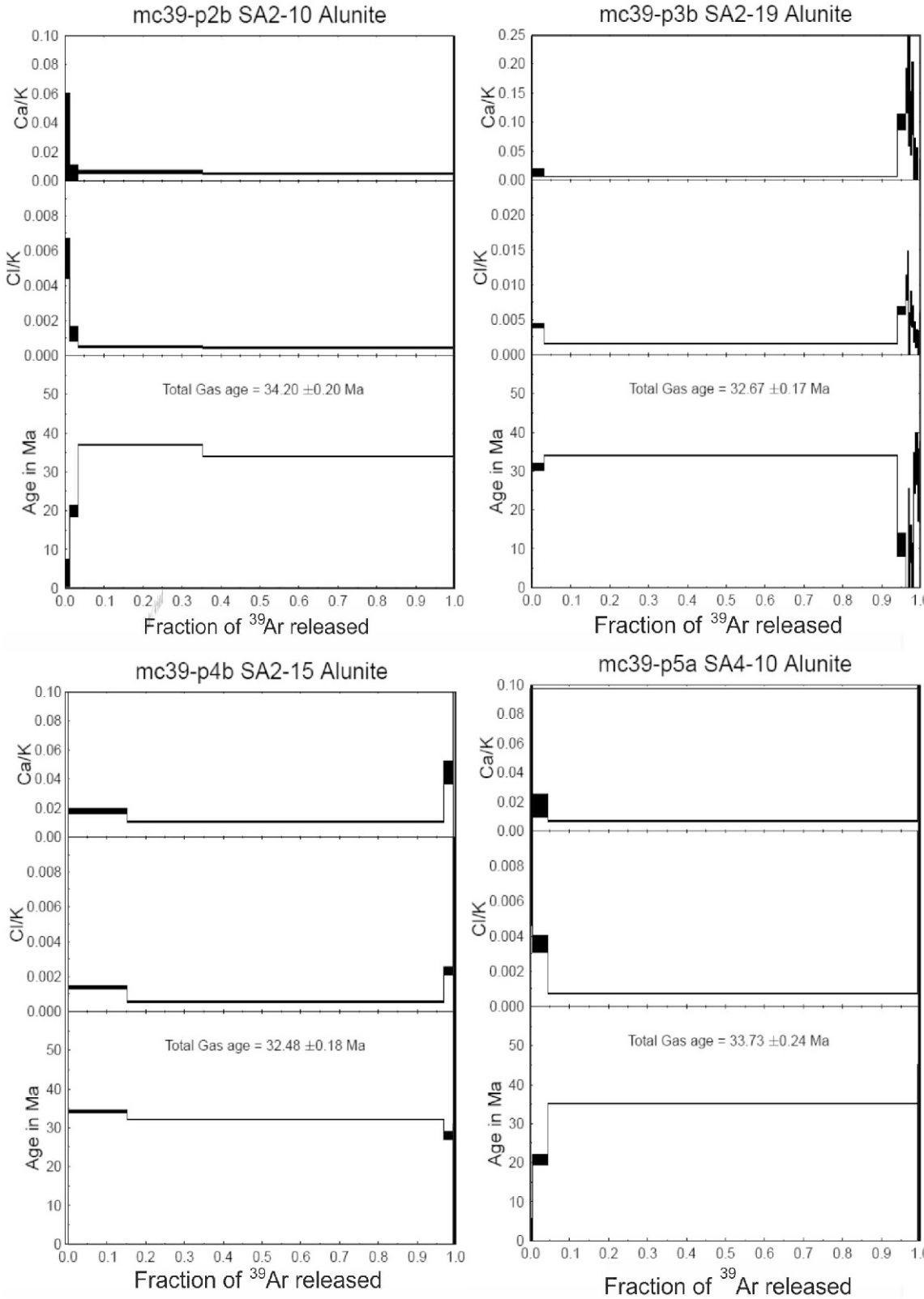

Figure 15. Ar-Ar age dating diagrams of alunite samples from the Sarıbeyli-Sığırlı deposit. The stepwise release of ^{39}Ar gives total gas ages that range from 32.5 to 34.2 Ma, which corresponds to the Eocene–Oligocene boundary.

https://doi.org/10.1346/CCMN.2016.0640305 Published online by Cambridge University Press

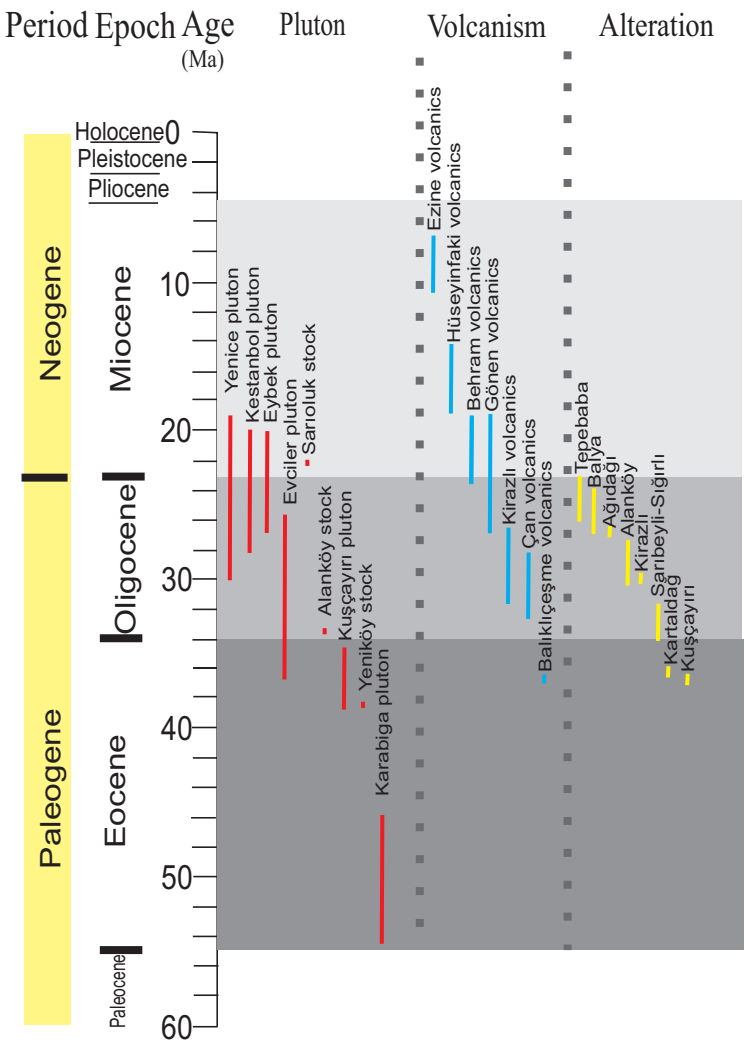

Figure 16. Relationship between Cenozoic magmatism and epithermal mineralization in the Biga Peninsula. A total of 109 radiometric age data; 3 × Re/Os, 32 × Ar/Ar, 71 × K/Ar, 2 × Rb/Sr, and 1 × U/Pb (Fytikas *et al.*, 1976; Birkle and Satır, 1995; Ercan *et al.*, 1995; Aldanmaz *et al.*, 2000; Delaloye and Bingöl, 2000; Beccaletto *et al.*, 2005; Murakami *et al.*, 2005; Kaymakçı *et al.*, 2007; Karacık *et al.*, 2008; and the present study). The geologic time scale is from Gradstein *et al.* (2004) and Table 5 is modified from Yiğit (2012, figure 6).

hydrothermal fluids ascending along the fracture zones, which silicified thise rocks having permeability and porosity greater than those of the pre-existing tuffs. Pre-existing tuff textures were controlled by such factors as gas content, thickness, and cooling history of the original deposit. Six pervasive siliceous sinter zones were found and each zone was about 20–40 cm wide. Morphological investigation of quartz within the fractures revealed they consist of grains that were up to 500 μm in diameter, with spaces between the quartz crystals filled with goethite and trace sulfate minerals. Kaolinized zones have high S (379–1548 ppm), Ba (up to 2054 ppm), and Fe_2O_3 (up to 12.63 wt.%) contents and anomalously high concentration of Cu (up to 163 ppm) and up to 2 ppm Au (Table 2).

Zone B-*ii* contained (in order of abundance) kaolinite + quartz ± alunite ± jarosite ± halloysite. This assemblage occurred very close to the silicified fault zones and was also controlled principally by the six fractures. The kaolinized zones were found between the fracture zones and spaced by about 5 to 15 m. Kaolinite was the most common mineral and occurred as randomly scattered crystals with dimensions that varied between 400–1500 nm (Figure 12c,d). Book-shaped kaolinite crystals had dimensions similar to the scattered crystals. Halloysite was characterized by tube morphologies with

https://doi.org/10.1346/CCMN.2016.0640305 Published online by Cambridge University Press

poorly defined internal lumen and with outer diameter of 45–200 nm. Some halloysite tubes displayed a spiral-like or serrated shape, suggesting they were undergoing transformation to kaolinite (Figure 12f).

Minor alunite- and jarosite-bearing samples taken near the fracture zones had additional kaolinite, halloysite, and quartz intergrowths. Sulfate concentrations decreased laterally away from fracture zones. The semi-quantitative XRD analyses of bulk samples indicated they comprise up to ~70 wt.% kaolinite and up to ~30 wt.% α-quartz. Where the silicification was more intense, samples contained up to 15 wt.% jarosite and up to 10 wt.% alunite. Kaolinite-rich samples contained high amounts of Al_2O_3 (up to 36.8 wt.%) and low amounts of Na_2O, Ca_2O, and K_2O (Table 2). These samples also have anomalously high concentrations of Au (up to 2.5 ppm), Ba (up to 2054 ppm), and S (up to 1548 ppm) when compared to other facies.

Zone B-*iii* contained (in order of abundance) kaolinite + halloysite + illite + quartz + montmorillonite. This mineral assemblage occurred in the areas where the intensity of hydrothermal alteration decreased laterally and the primary rock textures were still preserved. Kaolinite-rich samples contained up to 15 wt.% illite, montmorillonite, and halloysite. Halloysite minerals occurred in the fracture zones and anhedral quartz crystals were always found in this mineral assemblage.

Distinguishing hypogene from supergene alteration

Sillitoe (1993) distinguished deep and shallow epithermal systems by considering mineral compositions of the deposits and was the first to emphasize the significance of the position of the paleo-groundwater table above (giving rise to hot spring and sinter accumulations) or below (overprinting an acid-leached zone onto precious-metal-bearing veins) epithermal deposits (massive silicification in porous horizons) at the time of hydrothermal mineralization. Based on mineral assemblages of the Sarıbeyli-Sığırlı kaolin mineralization, two different hydrothermal stages were possible. At an early stage, the Sarıbeyli-Sığırlı kaolin deposits probably formed in relatively deep epithermal zones, as indicated by the presence of dickite, which is an indicator of high-temperature mineralization (according to Sillitoe's (1993) model, the groundwater table was below the mineralized zone). At a late stage, silicification took place mostly within tuffs, due to fluctuation of the paleo-groundwater table or/and the influence of cool meteoric water in the vicinity of upflowing geothermal waters close to the surface (according to Sillitoe's (1993) model, the groundwater table was above the mineralized zone). Alunite and kaolin group minerals typically occur under highly acidic and oxidizing conditions, typically surrounding silicic cores, in a high-sulfidation environment (Berger and Henley, 1989; Hedenquist *et al*., 2000). The position of the paleo-water table in the study areas was assumed to be falling during kaolinization, leaving an acid-leached zone above. This is because the silicified zone was minimally developed along the fault zones as late stage hydrothermal products. The assemblage of quartz + alunite + kaolinite + pyrite develops from the geothermal waters where pH's are usually between 2 and 4, as noted by Hemley *et al*. (1969), Stoffregen and Alpers, (1987), Rye *et al*. (1992), Harris *et al*. (1999), and Deyell *et al*. (2005). This gradient from low pH at depth to neutral pH near the surface makes possible the precipitation of silica as acids are consumed and more alkaline conditions prevail. Silica derived from other rock-forming silicates in deep conditions, especially from the feldspar group, dissolve in acidic conditions and the resulting orthosilicic acid is transported along with geothermal waters. The resulting hypothesis is that alunite, kaolinite, and amorphous silica precipitated at different episodes of the major hydrothermal activity, and the pH of geothermal waters changed from highly acidic to neutral. Consequently, previously altered volcanic rocks were further silicified along fault zones during the latest stage, which is supported by lepispheres lining pore cavities as seen in FE-SEM images (Fig. 12b). The XRD analysis of kaolinite shows disordered forms that usually occur at low temperatures (Bailey, 1993). In contrast, well ordered dickite occurs at high temperatures in the epithermal systems (Sillitoe, 1993). Alunite-rich samples with associated halloysite indicate acidic environments (Ece *et al*., 2008). Kaolinite-montmorillonite and quartz assemblages indicate pH 5 to 6 in the modern geothermal systems (Reyes, 1990), and therefore mineral associations suggest that hydrothermal fluids had laterally neutralized through interaction with the host rock.

Crystal sizes and shapes are also informative in paleo-environmental interpretations. High-temperature steam-heated environments have fine-grained alunite (<20 μm) and are associated with kaolinite and opal (Simón *et al*., 2005). Alunites typically found in the low-temperature and steam-heated environments have grain sizes of 20–50 μm, whereas grain sizes of hypogene alunites are coarse and in the range of 50 to 100 μm (Thompson *et al*., 1999; Hedenquist *et al*., 2000). Particles of alunites are up to 9 μm in both the Sarıbeyli-Sığırlı and Bodurlar deposits, where they are also intimately intergrown with kaolin group minerals and α-quartz. This suggests that alunite in the Sarıbeyli-Sığırlı deposit formed at relatively low-temperature in a steam-heated environment.

Silicified rocks along the fault zones indicate the feeders, as seen in Figure 3. Montmorillonite + illite + K-feldspar alterations occurring proximal to silicic zones suggests weakly acidic and near-neutral pH conditions. Such fluid-dominated hydrothermal systems represent neutral alkali-chloride conditions overlain by a steam-heated, acid-sulfate environment (Simón *et al*. 2005). The Sarıbeyli-Sığırlı deposits can be classified as acid-

https://doi.org/10.1346/CCMN.2016.0640305 Published online by Cambridge University Press

sulfate type (using older terminology of Heald *et al*., 1987) or alunite-kaolinite type high-sulfidation systems (using newer terminology of Hedenquist *et al*., 2000). An acid-sulfate type system may have formed on the flank of a low-sulfidation system. The intensity of alteration decreases away from fault zones where quartz, kaolinite, and alunite decrease, and montmorillonite increases outward from the fault systems. The permeability of the host rock Sarıbeyli-Sığırlı volcanics may have been greater than that of the Bodurlar volcanic rocks, which led to a more pervasive alteration.

Ece and Nakagawa (2003) and Ece *et al*. (2013) observed differential element mobility during acid-sulfate alteration of other Turkish hydrothermal kaolin deposits. High-field-strength elements (HFSE), such as Ti, Zr, Nb, and Y, are relatively immobile during hypogene alteration, whereas during supergene alteration Al, heavy *REE* (Lu, Yb), Hf, Ta, Th, and in some cases V and Cr are relatively immobile. Deposits affected by hypogene processes have relatively low Cr and Nb content (Dill and Bosse, 2000). The Sarıbeyli-Sığırlı kaolinized zones have high Ba + Sr concentrations above 2,000 ppm and low Ce + Y + La concentrations (<150 ppm) (Figure 17a). These elements are largely sourced from K-feldspars, which undergo dissolution in the initially undersaturated geothermal solutions. Using the classification scheme of Dill *et al*. (1997), the majority of Sarıbeyli-Sığırlı samples fall in the hypogene area and the Bodurlar samples fall in the mixed and supergene areas. Distinguishing supergene effects can be further understood using a Zr *vs.* TiO_2 binary diagram (MacLean and Barrett, 1993). Figure 17b shows these values for the Sarıbeyli-Sığırlı deposit, which fall in all three areas, whereas Bodurlar samples only fall in hypogene and mixed type environment areas.

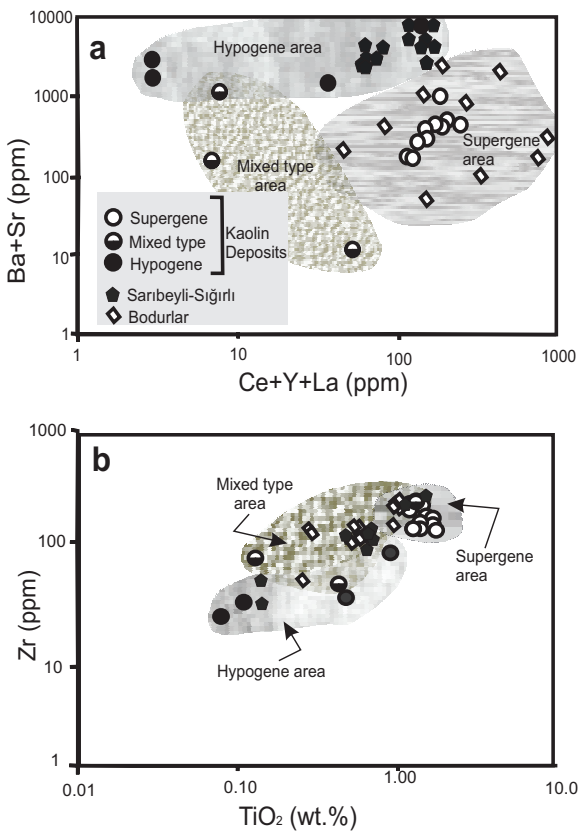

Figure 17. (a) Ce + Y + La *vs.* Ba + Sr plot of kaolin samples from the Sarıbeyli-Sığırlı and Bodurlar deposits. (b) Zr *vs.* TiO_2 plot of kaolinite samples from the Sarıbeyli-Sığırlı and Bodurlar deposits. Both plots show comparisons of the Sarıbeyli-Sığırlı and the Bodurlar kaolin deposits with Peruvian kaolin deposits (colored areas in the online version) (Dill *et al.*, 1997).

Some samples from Sarıbeyli-Sığırlı showed enrichment in As, Ba, Pb, Zr, V, Hg, and Sb. The transport of Hg was assumed to be as a vapor phase (Barnes and Seward, 1997). Hg contents ranged from 0.07 to 0.33 ppm in kaolin-rich samples and from 0.03 to 0.89 ppm in alunite-rich samples (Table 1). A study of the Rotokawa geothermal field, New Zealand, (Krupp and Seward, 1990) showed that the concentration of Hg in hydrothermal solutions was controlled by the solubility of Hg^0 above 250ºC and by the solubility of HgS at lower temperatures. Barnes and Seward (1997) indicated, however, that Hg^0 was possibly a dominant species at lower temperatures in steam-heated environments. The thermodynamic stability fields of the mercury sulfide complexes at 100ºC suggest that the solubility of $Hg(HS)_2$ is pH-dependent and favored below a pH of 6, whereas $HgS(HS)^-$ is favored between pH's 5.9 to 8.3, and Hg^0 above a pH of 8.3 These relations could explain why Hg concentrations vary spatially, as geothermal fluids evolved to increasing pH with time in the areas of maximum alteration (*i.e.* in the fault zones).

The stable isotopic data ($\delta^{34}S$, $\delta^{18}O$, and δD) for the Sarıbeyli-Sığırlı deposit suggest that it likely formed in a steam-heated environment, where H_2S-rich magmatic steam was condensed in the paleo water table and mixed with meteoric water, was cooled, and then oxidized and acidified (Schoen *et al*., 1974). Model calculations of formation temperature from kaolinites are between 66ºC and 118ºC. Some kaolin samples appear to be in equilibrium with meteoric water at the temperature of 35ºC. The dickite-rich sample produced a model formation temperature of 79ºC, which was lower than the >120ºC seen in other geothermal systems (Reyes, 1990). Dickite may have formed at >120ºC from mixing a small component of magmatic with meteoric water and then re-equilibrated isotopically (Simón *et al*., 2005) in the 70–80ºC in the steam heated environment. Kaolinite-to-dickite is considered an irreversible reaction, which is kinetically controlled. It proceeds by gradual structural changes concomitant to crystal coarsening and changes from booklet to blocky morphology, as seen in deeply buried sandstone (Beaufort *et al*.,

https://doi.org/10.1346/CCMN.2016.0640305 Published online by Cambridge University Press

1998). Although the kinetics are not exactly the same as in a hydrothermal system, crystallization of dickite is possible by either dissolution of small kaolinite crystals or feldspars ± micas that grow on early-formed coarser metastable kaolinite crystals by a dissolution-crystallization process.

During burial diagenesis, Beaufort *et al*. (1998) noted that the kaolinite-to-dickite transition in sandstones occurs with increasing depth (and temperature) over the interval from 3000 m to 5000 m in the North Sea, corresponding to a model temperature range of 100 and 165ºC. In their case, the dehydroxylation TGA/DTA endotherm of kaolins progressively shifted from 525ºC (disordered kaolinite) towards 670ºC (dickite) *via* intermediate structures. Similar observations in depth-dependent transformation of kaolinite-to-dickite in sandstones of the Norwegian continental shelf have been documented by Ehrenberg *et al*. (1993). Besides, Brindley and Porter (1978) reported that DTA curves of dickites differ remarkably from those of kaolinites in the temperature range 500−700ºC where dehydroxylation occurs in the Job's Hill geothermal field, St. Mary, Jamaica. Kaolinites show a single endotherm which is more or less sharp with a peak temperature around 550−600ºC. The Gibbs free energy of the reaction kaolinite ↔ dickite was generated from solubility measurements of natural kaolinite and dickite performed in acid solutions at temperatures ranging from 150 to 300ºC under vapor-saturated conditions (Zotov *et al*., 1998). This supports the idea that acid-sulfate alteration conditions are present in the Sarıbeyli-Sığırlı geothermal fields and that the dickite formed at higher temperatures than kaolinite in the Bodurlar field.

The Bodurlar deposits are characterized by an assemblage similar to Sarıbeyli-Sığırlı, containing, quartz + kaolinite + halloysite + alunite, but also + jarosite. Alunite was probably the product of an early-to-intermediate alteration stage because of close association with halloysite, which crystallized before kaolinite (Figure 13). These minerals formed under the influence of intense feldspar dissolution at a pH of 2 and at an oxygen fugacity slightly above the thermodynamic boundary between the H_2S and bisulfate fields. The temperature of formation was in the range of 200 to 450ºC during this alteration, consistent with the work of Stoffregen (1987) suggesting around 250ºC. This temperature was much higher than the model formation temperature, which was calculated to be 40−65ºC, based on kaolinite O isotope values. These temperatures are similar to those in the range of 39−55ºC found experimentally by Simón *et al*. (2005). If Hg was transported in a steam-heated system, then temperatures must have been greater than 100ºC. These lower temperatures were then possibly related to a steam-heated process, which condensed waters in the vadose zone, mixed with meteoric water, and then isotopically re-equilibrated.

Wide ranges of temperature gradients have been proposed during the formation of alunite and silica (Stoffregen, 1987; Hedenquist *et al*., 1994; Wang, 2010). Fluid inclusion measurements in alunite-silica alteration zones suggest that alunite is stable up to at least 450ºC (Stoffregen, 1987). Thermodynamic data (Hemley *et al*., 1969, 1980) also suggest that when strongly acidic solutions react with volcanic tuffs and rocks, it results in high dissolved silica activity (Fournier, 1985; Africano *et al*., 2002). The silica activity−temperature relations of metastable polymorphs of silica precipitating together with alunite or with kaolinite at 250 bar vapor pressure between 225º to 550ºC are well documented (figure 2 in Henley and Berger, 2011). During the cooling process, near the surface, metastable silica transitions through a sequence of polymorphs from opal-A, opal-CT, and quartz (Africano and Bernard, 2000; Okamoto *et al*., 2010), resulting in massive, very thick, highly silicified rocks, including "vuggy silica" on pore surfaces, where groundwater infiltrates.

The occurrence of pseudo-hexagonal alunite crystals and the subsequent forming of halloysite tubes is a function of difference in water pH and the porosity and permeability of the parent rocks. The proposed paragenetic sequence can be visualized on the right side of Figure 13. Transformation dynamics of halloysite to kaolinite during weathering likely proceed by a dissolution and recrystallization mechanism, which has been proposed by Steefel and van Cappelen (1990), Fritz *et al*. (2009), and Fritz and Noguera (2009). The transformation of halloysite to kaolinite (Figure 12f, g) was seen by the occurrence of curved kaolinite flakes (Figure 12d), which results when incipient thin-layered crystals are stressed in part by the misfit between octahedral and tetrahedral sheets resulting in curling strain. Two models have been proposed to explain the transformation from halloysite to kaolinite (H-to-K) during weathering: (1) dissolution and recrystallization and (2) rolling and unrolling models (Churchman, 2000; Joussein *et al*., 2005; Churchman and Lowe, 2012). Fresh, unweathered granite samples were not exposed, thus indicating the granite was exhumed by weathering. The Bodurlar kaolin deposits reveal a pattern of a weathering profile derived from compositionally similar granitic parent rocks, where halloysite forms early and kaolinite forms later in the same profile (Tardy, 1982; Churchman, 2000; Churchman and Lowe, 2012). The solubility of halloysite is greater than kaolinite under meteoric weathering conditions (Su and Harsh, 1994; Inoue *et al*. 2012), which is supported by the difference in measured Gibbs free energy of kaolinite (−3799.4 kJ/mol) *vs.* halloysite (−3780.7 kJ/mol) at 25ºC. Halloysite is a fast-forming metastable precursor to kaolinite (Joussein *et al*., 2005; Su and Harsh, 1994). Inoue *et al*. (2012) demonstrated that halloysite crystallizes prior to kaolinite *via* precipitation from solution with progressive weathering of feldspars, and early-

https://doi.org/10.1346/CCMN.2016.0640305 Published online by Cambridge University Press

formed halloysite transforms to kaolinite following Ostwald's step rule. The shrinkage of pores caused by dehydration increases surface area, which further promotes dissolution upon rehydration. Inoue *et al*. (2012) pointed out that kaolinite nucleates and grows heterogeneously on the edges of halloysite tubes. This is clearly shown in Figure 12.

The $^{40}Ar/^{39}Ar$ ages of the various rock types and alunite, and the summary of other radiometric age data of magmatic rocks in the vicinity of the study area and the Biga Peninsula, are listed in Table 5 and illustrated in Figure 16. Based on available radiometric age dating data of whole-rock, biotite, and K-feldspar from granite, granodiorites, and andesites in the Biga Peninsula, the temporal relations of the plutonism, volcanism, and hydrothermal episodes of mineralization are summarized in Figure 16. The radiometric data support the notion that calc-alkaline plutonism was active from Early Eocene to Early Miocene. Volcanic compositions follow almost the same pattern from Early Oligocene to Late Miocene and hydrothermal alterations were active from Late Eocene through Oligocene. The findings here of Ar-Ar alunite dates (Table 5) are consistent with the hydrothermal alteration dates from primary volcanic rocks (see references in Figure 16). These findings indicate that the alunite at both deposits most probably formed during igneous hydrothermal activity. Close spatial and temporal relationships between magmatic activities are observed in and throughout Western Turkey (Altunkaynak and Yılmaz, 1998, 1999; Yılmaz *et al*., 2001; Altunkaynak *et al*., 2010; Altunkaynak *et al*., 2012a, 2012b; Çoban *et al*., 2012; Altunkaynak and Dilek, 2013). The calc-alkaline magmatic activity waned during the mid-Miocene, although during the Late Miocene, widely distributed hydrothermal metal mineralization occurred in many areas of the Biga Peninsula (Altunkaynak and Dilek, 2006; Altunkaynak and Genç, 2008; Yiğit, 2012).

Differences in oxygen and hydrogen isotopes of the kaolin group minerals can also be used to distinguish the effects of hypogene and supergene alteration. Both the Sarıbeyli-Sığırlı and Bodurlar deposits have mineral zones that indicate igneous-related hydrothermal activity in the supergene environments. Component calculated model formation temperatures of the Bodurlar deposit are between 39 and 54ºC, thus reflecting isotopic re-equilibrium with meteoric water in the supergene environment. The calculated model temperatures of the Sarıbeyli-Sığırlı deposits range from 79 to 106ºC, thus reflecting temperatures of the fossil geothermal fields, similar to the Turplu halloysite deposits to the south (Ece *et al*., 2008). The Sarıbeyli-Sığırlı deposits likely formed in a hypogene environment, and isotopic data plot very close to the line representing kaolinites in equilibrium with meteoric waters at 100ºC. Figure 14 shows that halloysite δD and $\delta^{18}O$ values can distinguish between their supergene or hypogene origin. The area to the left of the S/H line indicates a hypogene origin (*i.e.* Sarıbeyli-Sığırlı deposits), whereas the areas to the right-hand side indicate a supergene environment (*i.e*. Bodurlar deposits). Moreover, these hydrothermal kaolin deposits were further evolved by interactions with meteoric water during the post-mineralization period. Isotopic re-equilibrium reflects a lower temperature resulting in halloysites being slightly enriched in $\delta^{18}O$ and highly enriched in δD (Garvelmann *et al*., 2012). They demonstrated porewater-based ratios of deuterium (^2H) to hydrogen (^1H) as natural tracers in order to explore hydrological processes at the hillslope in a humid mountainous catchment in Germany and found that δD ($=\delta^2H$) values are continuously lighter with increasing soil depth as the result of the precipitation falling during the winter with the lightest deuterium values. The vertical deuterium depth profiles show a typical seasonal pattern: soil water stemming from summer rainfall near the surface and an increasing proportion of soil water from winter precipitation with increasing soil depth. The results of Garvelmann *et al*. (2012) suggest a vertical movement of soil water at upslope positions, indicated by a preservation of the seasonal precipitation trend in the subsurface. These studies showed that H atoms have a greater tendency for isotope exchange during the post-mineralization period due to smaller ionic radius. In the study area, the parent rocks are tuffs containing large amounts of amorphous material and have more porosity and permeability than other volcanic and intrusive rocks. For this reason, the alteration of tuffs takes place faster than the alteration of other magmatic rocks in these epithermal environments.

All field and laboratory studies are summarized in Figure 18, which is a schematic diagram showing a high-sulfidation epithermal model proposed for the occurrence of kaolinite, halloysite, and alunite deposits in this study. The details of a similar, high-sulfidation epithermal model, from the Düvertepe hydrothermal kaolin deposits of the Simav graben in the Western Anatolia, have been discussed previously (Ece *et al*., 2013). Inferred properties of Si-rich geothermal waters that caused silicification of volcanic rocks in upflow areas along fault zones in the fossil hydrothermal systems are illustrated in this conceptual geological model (Figure 18). The zonation of mineral assemblages from proximal to distal facies and the significance of the position of paleo-water level during the kaolinitization period are likely factors in the paragenetic sequence of mineralization (Figures 13 and 18). Fournier and Potter (1982) noted that quartz-saturated water at 200ºC (~265 mg/l SiO_2) can be enriched in silica through additional contact with α-cristobalite (solubility ~464 mg/L SiO_2) occurring in overlying volcanics. This translates to 1 g of quartz precipitating for every ~5 L of geothermal water. The silica sinters on the surface in both deposits lie within the fault zones, which suggest that large amounts of acidic geothermal waters carried dissolved silica.

https://doi.org/10.1346/CCMN.2016.0640305 Published online by Cambridge University Press

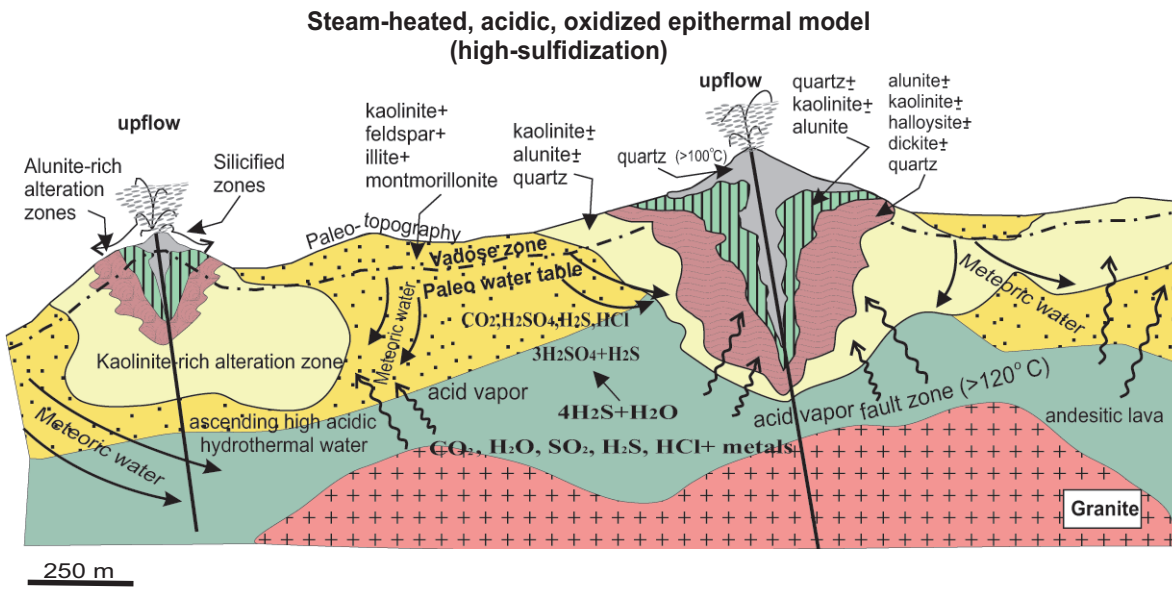

Figure 18. The proposed epithermal, high-sulfidation, and steam-heated geologic model explains the origin of high-sulfidation systems in the Sarıbeyli-Sığırlı and the Bodurlar kaolin deposits. Modified from Henley and Ellis (1983), Heald *et al*. (1987), and Cortecci *et al*. (2001).

Lastly, the kaolinite-to-dickite transformation was controlled mostly by temperatures nearing the onset of hypogene conditions (>100ºC) or dickite may have been neoformed from dissolution of feldspar. The peak TGA dehydroxylation values indicate the approximate proportion of kaolinite in kaolinite/dickite mixed-layer samples presented here and this value is supported by diagenetic studies of sandstones in Spain (Ruiz Cruz and Moreno Real, 1993). Both textural and structural data (*e.g.* see TEM data in Figure 9e) show that the kaolinite-to-dickite reaction proceeds gradually with crystal growth through dissolution-crystallization over a wide range of increasing hydrothermal gradients. Initial kaolinite crystals begin to undergo structural changes under higher thermal conditions to form disordered dickite (Beaufort *et al*., 1998). The kaolinite-to-dickite reaction requires only low apparent activation energy for kaolinite dissolution. During the later stages of hypogene acid-sulfate dissolution processes of tuffs and volcanic rocks, most of the Al-bearing, framework silicates are dissolved and the only source of Al and Si for the dickite growth is the dissolution of the finer particles of kaolinite. The amount of neoformed dickite will be strongly temperature dependent given the high activation energy. These observations suggest that the formation temperature in the Sarıbeyli-Sığırlı was higher than in the Bodurlar kaolin deposit. Relative differences in crystal structures are compared between Sarıbeyli-Sığırlı and the Bodurlar kaolin deposits, based on difference in the formation temperatures, porosity and permeability of parent rocks, and the chemistry of geothermal waters. Although the values of isotopic compositions and mineral crystal chemistry are not absolute, the relative trends provide a guideline for comparing other altered volcanic rocks that may have been modified by both hypogene and supergene processes to varying degrees.

CONCLUSIONS

Crystal chemical, isotopic, and radiometric study of two proximal kaolin deposits in NW Turkey hosted in similar parent rocks suggests each deposit experienced different degrees of hydrothermal and meteoric alteration processes. The most economic primary kaolin deposits possibly experienced overprinting from the meteoric waters differentially heated by hydrothermal processes. The resulting mineral assemblages observed in the Sarıbeyli-Sığırlı and Bodurlar deposits provide good examples of criteria that can be used to help distinguish the relative extent of supergene and hypogene alteration present in epithermal kaolin deposits. The Sarıbeyli-Sığırlı and Bodurlar deposits were assumed to be differently zoned and controlled by proximity and density of faulting and by initial permeability of the volcanic rocks. Discriminating crystal-chemical features were found in the Sarıbeyli-Sığırlı and Bodurlar deposits (Table 6). These include such features as (1) crystal habits, (2) isotopic and elemental enrichments or depletions, (3) thermal properties, and (4) kaolin group structure properties as measured by XRD and vibrational spectroscopies. The purpose of comparing and contrasting these properties from the two Turkish deposits was to provide guidelines for the study of primary kaolin deposits formed from volcanic rocks, realizing that no absolute criteria exist for differentiating hypogene and supergene influences. In practice, deposits

https://doi.org/10.1346/CCMN.2016.0640305 Published online by Cambridge University Press

Table 6. Relative criteria for distinguishing the extent of hypogene *vs.* supergene alteration in primary kaolin deposits of NW Turkey.

Distinguishing criteria	Hypogene Sarıbeyli-Sığırlı deposit	Supergene Bodurlu deposit
Halloysite crystal habits	Well formed tubes	Serrated tubes
Kaolinite crystal habits	Blocky and vermiform	Curved edges
Halloysite to kaolinite transformation	Not observed	Common
Dickite crystal habits	Thicker	Thinner
Feldspar dissolution	Arched edges	Early stage of formation of halloysite tubes
Alunite crystal habits	Euhedral <10 μm	Dissolution pits
Silica sinter	Abundant on surface	Abundant within fault zones
Quartz crystal habits	Subhedral, 1.5–6 μm	Lepispheres, drusy
$\delta^{18}O$ *vs.* δD of kaolins	$\delta^{18}O$ depleted-δD enriched	$\delta^{18}O$ enriched-δD depleted
(Ba+Sr) *vs.* (Ce+Y+La)	Large slope	Small slope
Zr and TiO_2 concentrations	Low	High
Kaolin DTA % weight loss ratio of endotherm maxima ~575ºC/~658ºC	Low	High
XRD reflection intensities 1.3160 Å/1.3069 Å	High	Low
FTIR (O–H stretch band) 3620/3652 cm^{-1} absorbance intensity ratio	Low	High
Raman (O–H stretch band) ratio of ν_{1a} to ν_5 intensities	Low	High

may often have overprinting, thus making difficult a unique classification. The features listed for the Sarıbeyli-Sığırlı and Bodurlar deposits, however, do serve as a references to gauge the properties of other deposits worldwide. Given that multiple processes are responsible for the formation of hydrothermal kaolin and alunite deposits, these criteria are not expected to be exactly the same for all alunite deposits. However, the general trends and relative crystal-chemical, isotopic, and radiometric observations made in the current study can be used as guidelines for understanding the degrees of hypogene and supergene alteration experienced by economic kaolin deposits.

ACKNOWLEDGMENTS

This research was made possible with the support of TÜBİTAK-ÇAYDAG Project No: 112Y369 (Ö.I. Ece). Additional support was obtained from the Istanbul Technical University Research Fund (BAP Project No: 34778) (Ö.I. Ece). The authors express gratitude to Dr. İsmail Koyuncu for providing technical support during FE-SEM studies in Istanbul Technical University (ITU), to Dr. Doug Crowe for stable isotope analyses at the University of Georgia, Athens, USA, to Chris Hall for $^{40}Ar/^{39}Ar$ studies in the University of Michigan, Ann Arbor, USA, and to Dr. Muhammed Bekin for Raman spectroscopy studies in the MEMTEK-ITU laboratory, Turkey. Also, they are grateful to Kalemaden Mining Corp. for its logistical support and accommodations during the fieldwork in the summers of 2011 and 2013. The authors appreciate productive comments of reviewer, Dr. Özcan Yiğit.

REFERENCES

Acarlioğlu, S., Kadir, S., Abdioğlu, E., and Arslan, M. (2012) Epithermal-alteration geology, mineralogy and geochemistry of Eocene volcanic rocks in the Hasandağ (Giresun) area, eastern Pontides, NE Turkey. *Neues Jahrbuch für Mineralogie*, **190**, 79–99

Africano, F. and Bernard, A. (2000) Acid alteration in the fumarolic environment of Usu volcano, Hokkaido, Japan. *Journal of Volcanology and Geothermal Research*, **97**, 475–495.

Africano, F., van Rompaey, G., Bernard, A., and Le Guern, F. (2002) Deposition of trace elements from high temperature gases at Satsuma-Iwo Jima volcano. *Earth, Planets and Space*, **54**, 275–286.

Ağdemir, N., Kırıkoğlu, M.S., Lehmann, B., and Tietze, J. (1994) Petrology and alteration geochemistry of the epithermal Balya Pb–Zn–Ag deposit, NW Turkey. *Mineralium Deposita*, **29**, 366–371.

Aldanmaz, E., Pearce, J.A., Thirlwall, M.F., and Mitchell, J.G. (2000) Petrogenic evolution of Late Cenozoic, post-collisional volcanism in western Anatolia, Turkey. *Journal of Volcanology and Geothermal Research*, **102**, 67–95.

Altunkaynak, Ş. and Dilek, Y. (2006) Timing and nature of post collisional volcanism in Western Anatolia and geodynamic implications. Pp. 321-351 in: *Post-Collisional Tectonics and Magmatism of the Eastern Mediterranean*

https://doi.org/10.1346/CCMN.2016.0640305 Published online by Cambridge University Press

Region (Y. Dilek and S. Pavlides, editor). Geological Society of America Special Paper, **409**, 321–351.

Altunkaynak, Ş. and Dilek, Y. (2013) Eocene mafic volcanism in northern Anatolia: Its causes and mantle sources in the absence of active subduction. *International Geology Review*, **55**, 1641–1659.

Altunkaynak, Ş. and Genç, Ş.C. (2008) Petrogenesis and time-progressive evolution of the Cenozoic continental volcanism in the Biga Peninsula, NW Anatolia (Turkey). *Lithos*, **102**, 316–340.

Altunkaynak, S. and Yılmaz Y. (1998) The Mount Kozak magmatic complex, Western Anatolia. *Journal of Volcanology and Geothermal Research*, **85**, 211–231.

Altunkaynak, S. and Yılmaz, Y. (1999) The Kozak Pluton and its emplacement. *Geological Journal*, **34**, 257–274.

Altunkaynak, Ş., Rogers, N.W., and Kelley, S.P. (2010) Causes and effects of geochemical variations in late Cenozoic volcanism in the Foça volcanic centre, NW Anatolia, Turkey. *International Geology*, **52**, 579–607.

Altunkaynak, Ş., Dilek, Y., Genç, C.Ş., Sunal, G., Gertisser, R., Furnes, H., Foland, K.A., and Yang, J. (2012a) Spatial, temporal and geochemical evolution of Oligo-Miocene granitoid magmatism in western Anatolia, Turkey. *Gondwana Research*, **21**, 961–986.

Altunkaynak, Ş., Sunal, G., Aldanmaz, E., Genç, C.Ş., Dilek, Y., Furnes, H., Foland, K.A., Yang, J., and Yıldız, M. (2012b) Eocene granitic magmatism in NW Anatolia (Turkey) revisited: New implications from comparative zircon SHRIMP U-Pb and $^{40}Ar/^{39}Ar$ geochronology and isotope geochemistry on magma genesis and emplacement. *Lithos*, **155**, 289–309.

Arslan, M., Kadir, S., Abdioğlu, E., and Kolaylı, H. (2006) Origin and formation of kaolin minerals in saprolite of Tertiary alkaline volcanic rocks, Eastern Pontides, NE Turkey. *Clay Minerals*, **41**, 597–617.

Bailey, S.W. (1993) Review of the structural relationships of the kaolin minerals. Pp. 25–42 in: *Kaolin Genesis and Utilization* (H.H. Murray, W.M. Bunday and C.C. Harvey, editors), Boulder, Colorado, USA. Clay Minerals Society, Special Publication **1**.

Balan, E., Delattre, S., Guillaumet, M., and Salje, E.K.H. (2010) Low-temperature infrared spectroscopic study of OH-stretching modes in kaolinite and dickite. *American Mineralogist*, **95**, 1257–1266.

Barnes, H.L. and Seward, T.M. (1997) Geothermal systems and mercury deposits. Pp. 699–736 in: *Geochemistry of Hydrothermal Ore Deposits* (H.L. Barnes, editor), 3rd edition. New York, John Wiley.

Beaufort, D., Cassagnabere, A., Petit, S., Lanson, B., Berger, G., Lacharpagne, J.C., and Johansen, H. (1998) Kaolinite-to-dickite reaction in sandstone reservoirs. *Clay Minerals*, **33**, 297–316.

Beccaletto, L., Bartolini, A.C., Martini, R., Hochuli, P.A., and Kozur, H. (2005) Biostratigraphic data from Çetmi Melange, northwest Turkey: Palaeogeographic and tectonic implications. *Palaeogeography, Palaeoclimatology, Palaeoecology* **221**, 215–244.

Berger, H. and Henley, R.W. (1989) Advances in understanding of epithermal gold-silver deposits, with special reference to the western United States. *Economic Geology* Monograph **6**, 405–423.

Birkle, P. and Satir, M. (1995) Dating, geochemistry and geodynamic significance of the Tertiary magmatism of the Biga Peninsula, NW Turkey. Pp. 171–180 in: *Geology of the Black Sea Region* (A. Erler, T. Ercan, E. Bingol, and S. Orcen, editors). General Directorate of Mineral Research and Exploration & Chamber of Geological Engineers, Ankara.

Bozzola, J.J. and Russell, L.D. (1999) *Electron Microscopy: Principles and Techniques for Biologists*. Jones and Bartlett Publishers, Boston, 670 pp.

Brindley, G.W. and Porter, A.R.D. (1978) Occurrence of dickite in Jamaica – ordered and disordered varieties. *American Mineralogist*, **63**, 554–562.

Brindley, G.W., Kao, C.C., Harrison, J.L., Lipsicas, M., and Raythatha, R. (1986) Relations between structural disorder and other characteristics of kaolinites and dickites. *Clays and Clay Minerals*, **34**, 239–249.

Churchman G.J. (2000) The alteration and formation of soil minerals by weathering. Pp. F3-F76 in: *Handbook of Soil Science* (M.E. Summer, editor), CRC press, Boca Raton, Florida, USA.

Churchman G.J. and Lowe D.J. (2012) Alteration, formation and occurrence of minerals in soils. Pp. 20.1-20.72 in: *Handbook of Soil Sciences. Properties and Processes*, 2nd edition (P.M. Huang, Y. Li, and M.E. Summer, editors), CRC press, Boca Raton, Florida, USA.

Çoban, H., Zekiye, Z., and Ece, Ö.I. (2012) Source contamination and tectonomagmatic signals of overlapping Early to Middle Miocene orogenic magmas associated with shallow continental subduction and asthenospheric mantle flows in Western Anatolia: A record from Simav (Kütahya) region. *Lithos*, **140**, 119–141.

Cortecci, G., Dinelli, E., Bolognesi, L., Boschetti, T., and Ferrara, G. (2001) Chemical and isotopic compositions of water and dissolved sulfate from shallow wells on Vulcano Island, Aeolian Archipelago, Italy. *Geothermics*, **30**, 69–91.

Dayal, A. (1984) Mineralogical and petrographic investigation of Yenice (Çanakkale) granite. [Ph.D. dissertation]: Izmir, University of Dokuz Eylül.

Delaloye, M. and Bingöl, E. (2000) Granitoids from western and northwestern Anatolia: Geochemistry and modeling of geodynamic evolution. *International Geological Review*, **42**, 241–268.

Deyell, C., Rye, R., Landis, G., and Bissing, T. (2005) Alunite and the role of magmatic fluids in the Tambo high-sulfidation deposit, El Indio Pascua belt, Chile. *Chemical Geology*, **215**, 185–218.

Dill, H.G. and Bosse, H.R. (2000) Mineralogical and chemical studies of volcanic-related Argillaceous industrial minerals of the Central American Cordillera (western El Salvador). *Economic Geology*, **95**, 517–538.

Dill, H.G., Bosse, H.R., Henning, K.H., Fricke, A., and Ahrendt, H. (1997) Mineralogical and chemical variations in hypogene and supergene kaolin deposits in a mobile fold belt – The Central Andes of northwestern Peru. *Mineralium Deposita*, **32**, 149–163.

Dill, H.G., Dohrmann, R., Kaufhold, S., and Balaban, S.I. (2015) Kaolinization - a tool to unravel the formation and unroofing of the Pleystein pegmatite–aplite system (SE Germany). *Ore Geology Reviews*, **69**, 33–56.

Ece, O.I. and Nakagawa, Z. (2003) Alteration of volcanic rocks and genesis of kaolin deposits in Sile region, northern Istanbul, Turkey. Part II. Differential mobility of elements. *Clay Minerals*, **38**, 529–550.

Ece, O.I., Nakagawa, Z., and Schroeder, P.A. (2003) Alteration of volcanic rocks and genesis of kaolin deposits in the Şile Region, Northern İstanbul, Turkey. Part I: Clay mineralogy. *Clays and Clay Minerals*, **51**, 675–688.

Ece, O.I. and Schroeder, P.A. (2007) Clay mineralogy and chemistry of halloysite and alunite deposits in the Turplu area, Balıkesir, Turkey. *Clays and Clay Minerals*, **55**, 18–35.

Ece, O.I., Schroeder, P.A., Smilley, M.J., and Wampler, J.M. (2008) Acid-sulfate hydrothermal alteration of andesitic tuffs and genesis of halloysite and alunite deposits in the Biga Peninsula, Turkey. *Clay Minerals*, **43**, 281–315.

Ece, O.I., Ekinci, B., Schroeder P.A., Crowe D., and Esenli F. (2013) Origin of the Düvertepe kaolin–alunite deposits in Simav Graben, Turkey: Timing and styles of hydrothermal

mineralization. *Journal of Volcanology and Geothermal Research*, **255**, 57–78.

Ehrenberg, S.N., Aagaard, P., Wilson, M.J., Fraser, A.R., and Duthie, D.M.L. (1993) Depth-dependent transformation of kaolinite to dickite in sandstones of the Norwegian continental shelf. *Clay Minerals*, **28**, 325–352.

Ercan, T. (1979) Cenozoic volcanism of Thrace and Aegean islands of the western Anatolia. *Geological Engineering Bulletin*, **9**, 23-46 (in Turkish).

Ercan, T., Satır, M., Steinitz, G., Dora, A., Sarifakioglu, E., Adis, C., Walter, H.J., and Yıldırım, T. (1995) Features of Tertiary volcanism observed at Biga Peninsula and Gökçeada, Tavşan Islands, NW Anatolia. *MTA Bulletin*, **117**, 55–86 (in Turkish).

Fournier, R.O. (1985) The behavior of silica in hydrothermal solution. Pp. 45–72 in: *Geology and Geochemistry of Epithermal Systems* (B.R. Berger and P.M. Bethke, editors), Society of Economic Geology Reviews in Economic Geology **2**.

Fournier, R.O. and Potter, R.W. (1982) A revised and expanded silica quartz geothermometer. *Geothermal Resource Council Bulletin*, **11**, 3–12.

Fritz, B. and Noguera, C. (2009) Mineral precipitation kinetics. Pp. 371–410 in: *Thermodynamics and Kinetics of Water-Rock Interaction* (E.H. Oelkers and J. Schott, editors). Reviews in Mineralogy and Geochemistry, **70**, Mineralogical Society of America, Chantilly, Virginia, USA.

Fritz, B., Clement A., Amal, Y., and Noguera, C. (2009) Simulation of the nucleation and growth of simple clay minerals in weathering processes: The NANOKIN code. *Geochimica et Cosmochimica Acta*, **73**, 1340–1358.

Frost, R.L. (1995) Fourier-Transform Raman spectroscopy of kaolinite, dickite and halloysite. *Clays and Clay Minerals*, **43**, 191–195.

Frost, R.L., Fredericks, P.M., Kloprogge, J.T., and Hope, G.A. (2001) Raman spectroscopy of kaolinites using different excitation wavelengths. *Journal of Raman Spectroscopy*, **32**, 657–663.

Fytikas, M., Giuliani, O., Innocenti, F., Marinelli, G., and Mazzuoli, R. (1976) Geochronological data on recent magmatism of the Aegean Sea. *Tectonophysics*, **31**, T29–T34.

Garvelmann, J., Külls, C., and Weiler, M. (2012) A porewater-based stable isotope approach for the investigation of subsurface hydrological processes. *Hydrology and Earth System Sciences*, **16**, 631–640.

Gradstein, F.M., Ogg, J.G., and Smith, A.G. (2004) *A Geologic Time Scale*. Cambridge University Press, 460 pp.

Harris, C., Compton, J.S., and Bevington, S.A. (1999) Oxygen and hydrogen isotope composition of kaolinite deposits, Cape Peninsula, South Africa: Low-temperature, meteoric origin. *Economic Geology*, **94**, 1353–1366.

Hatipoğlu, M., Helvacı, C., Chamberlain, S.C., and Babalık, H. (2010) Mineralogical characteristics of unusual "Anatolian" diaspore (zultanite) crystals from the İlbirdağı diasporite deposit, Turkey. *Journal of African Earth Sciences*, **57**, 525–541.

Hayba, D.O., Bethke, P.M., Heald, P., and Foley, N.K. (1985) Geologic, mineralogic, and geochemical characteristics of volcanic-hosted epithermal precious metal deposits. Pp. 129-167 in: *Geology and Geochemistry of Epithermal Systems* (B.R. Berger and P.M. Bethke, editors), Reviews in Economic Geology **2**.

Heald, P., Foley, N.K., and Hayba, D.O. (1987) Comparative anatomy of volcanic-hosted epithermal deposits; acid-sulfate and adularia-sericite types. *Economic Geology*, **82**, 1–26.

Hedenquist, J.W., Matsuhisa, Y., Izawa, E., White, N.C., and Giggenbach, W.F. (1994) Geology, geochemistry, and origin of high sulfidation Cu–Au mineralization in the Nansatsu District, Japan. *Economic Geology*, **89**, 1–30.

Hedenquist, J.W., Arribas, A., Jr., and Gonzales-Urien, E. (2000) Exploration for epithermal gold deposits. *Reviews in Economic Geology*, **13**, 245–277.

Hemley, J.J, Hostetler, P.B., Gude, A.J., and Mountjoy, W.T. (1969) Some stability relations of alunite. *Economic Geology*, **64**, 599–611.

Hemley, J.J., Montoya, J.W., Marinenko, J.W., and Luce, R.W. (1980) Equilibria in the system Al_2O_3–SiO_2–H_2O and some general implications for alteration/mineralization processes. *Economic Geology*, **75**, 210–228.

Henley, R.D. and Ellis, A.J. (1983) Geothermal systems ancient and modern: a geochemical review. *Earth-Science Reviews*, **19**, 1–50.

Henley, R.W. and Berger, B.R. (2011) Magmatic-vapor expansion and the formation of high-sulfidation gold deposits: chemical controls on alteration and mineralization. *Ore Geology Reviews*, **39**, 63–74.

Hillier, S., Brydson, R., Delbos, E., Fraser, T., Gray, N., Pendlowski, H., Phillips, I., Robertson, J., and Wilson, I. (2016) Correlations among the mineralogical and physical properties of halloysite nanotubes (HNT). *Clay Minerals*, DOI: 10.1180/claymin.2016.051.3.11

Hinckley, D.N. (1963) Variability in "crystallinity" values among the kaolin deposits of the coastal plain of Georgia and South Carolina. *Clays and Clay Minerals*, **11**, 229–235.

Hurst, V.J. and Pickering, S.M., Jr. (1997) Origin and classification of Coastal Plain kaolins, southeastern USA, and the role of groundwater and microbial action. *Clays and Clay Minerals*, **45**, 274–285.

Inoue, A., Utada, A., and Hatta, A. (2012) Halloysite-to-kaolinite transformation by dissolution and recrystallization during weathering of crystalline rocks. *Clay Minerals*, **47**, 373–390.

Johnston, C.T., Helsen, J., Schoonheydt, R.A., Bish, D.L., and Agnew, S.E. (1998) Single-crystal Raman spectroscopic study of dickite. *American Mineralogist*, **83**, 75-84

Joswig, W. and Drits, V.A. (1986) The orientation of the hydroxyl groups in dickite by X-ray diffraction. *Neues Jahrbuch für Mineralogie, Monatshefte*, **1**, 19–22.

Joussein, E., Petit, S., Churchman, G.J., Theng, B.K.G., Righi, D., and Delvaux, B. (2005) Halloysite clay minerals – a review. *Clay Minerals*, **40**, 383–426.

Justet, L. and Spell, T.L. (2001) Effusive eruptions from a large silicic magma chamber: the Bearhead Rhyolite, Jemez volcanic field, NM. *Journal of Volcanology and Geothermal Research*, **107**, 241–264.

Kadir, S. and Akbulut, A. (2009) Mineralogy, geochemistry and genesis of the Taşoluk kaolinite deposits in pre-Early Cambrian metamorphites and Neogene volcanites of Afyonkarahisar, Turkey. *Clay Minerals*, **44**, 89–112.

Kadir, S. and Kart, F. (2009) The occurrence and origin of the Söğüt kaolinite deposits in the Paleozoic Sarıcakaya granite-granodiorite complexes and overlying Neogene sediments (Bilecik, northwestern Turkey). *Clays and Clay Minerals*, **57**, 311–329.

Kadir, S., Erman, H., and Erkoyun, H. (2011) Mineralogical and geochemical characteristics and genesis of hydrothermal kaolinite deposits within Neogene volcanites, Kütahya (western Anatolia), Turkey. *Clays and Clay Minerals*, **59**, 250–276.

Karacık, Z., Yilmaz, Y., Pearce, J.A., and Ece, O.I. (2008) Petrochemistry of the south Marmara granitoids, northwest Anatolia, Turkey. *International Journal Earth Sciences*, **97**, 1181–1200.

Kaymakçı, N., Aldanmaz, E., Langereis, C., Spell, T.L., Gurer, O.F., and Zanetti, K.A. (2007) Late Miocene transcurrent tectonics in NW Turkey: evidence from paleomagnetism and $^{40}Ar/^{39}Ar$ dating of alkaline volcanic rocks. *Geological Magazine*, **144**, 379–392.

Kogel, J.E. (2014) Mining and processing kaolin. *Elements*, **10**,

189–193.
Krupp, R.E. and Seward, T.M. (1990) Transport and deposition of metals in the Rotokawa geothermal system, New Zealand. *Mineralium Deposita*, **25**, 73–81.
Krushensky R.D. (1975) Neogene calc-alkaline extrusive and intrusive rocks of the Karalar Yeşiller area, Northwest Anatolia, Turkey. *Bulletin Volcanologique*, **39**, 336–360.
MacLean, W.H. and Barrett, T.J. (1993) Lithogeochemical techniques using immobile elements. *Journal of Geochemical Exploration*, **48**, 109–133.
Moore, D.M. and Reynolds, R.C. (1989) *X-Ray Diffraction and the Identification and Analysis of Clay Minerals*. Oxford University Press, pp. 375.
Murakami, H., Watanabe, Y., and Stein, H. (2005) Re-Os ages for molybdenite from the Tepeoba breccia-centered Cu-Mo-Au deposit, western Turkey: Brecciation triggered mineralization. Pp. 805–808 in: *Mineral Deposit Research: Meeting the Global Challenge* (J. Mao and F.P. Bierlein, editors). Proceedings of the Eight Biennial SGA Meeting, Beijing, China.
Murray, H.H. (2000) Traditional and new applications for kaolin, smectite, and palygorskite: a general overview. *Applied Clay Science*, **17**, 207–221.
Murray, H., Bundy, W., and Harvey, C. (1993) *Genesis and Utilization of Kaolin*. Special Publication No **1**, The Clay Minerals Society, Boulder, Colorado, USA, 341 pp.
Nakamura, H., Sumi, K., Katagiri, K., and Iwata, T. (1970) The geological environment of Matsukawa geothermal area, Japan. *Geothermics*, **2**, 221–231.
Okamoto, A., Saishu, H., Hirano, N., and Tsuchiya, N. (2010) Mineralogical and textural variation of silica minerals in hydrothermal flow-through experiments: implications for quartz vein formation. *Geochimica et Cosmochimica Acta*, **74**, 3692–3706.
Plançon A., Giese, R.F., and Snyder, R. (1988) The Hinckley index for kaolinites. *Clay Minerals*, **23**, 249–260.
Reyes, A.G. (1990) Petrology of Philippine geothermal systems and the application of alteration mineralogy to their assessment. *Journal of Volcanology and Geothermal Research*, **43**, 279–309.
Ruiz Cruz, M.D. and Moreno Real, L. (1993) Diagenetic kaolinite/dickite (Betic Cordilleras, Spain). *Clays and Clay Minerals*, **41**, 570–579.
Rye, R.O., Bethke, P.M. and Wasserman, M.D. (1992) The stable isotope geochemistry of acid sulfate alteration. *Economic Geology*, **87**, 225–255.
Schoen, R., White, D.E., and Hemley, J.J. (1974) Argillization by descending acid at Steamboat Springs, Nevada. *Clays and Clay Minerals*, **22**, 1–22.
Schroeder, P.A. and Erickson, G. (2014) Kaolin: From ancient porcelains to nanocomposites. *Elements*, **10**, 177–182.
Sengör, A.M.C. (1979) Mid-Mesozoic closure of Permo–Triassic Tethys and its implications. *Nature*, **279**, 590–593.
Şengör, A.M.C. and Yılmaz, Y. (1981) Tethyan evolution of Turkey: a plate tectonic approach. *Tectonophysics*, **75**, 181–241.
Seyitoglu, G. and Scott, B.C. (1992) Late Cenozoic volcanic evolution of the northeastern Aegean region. *Journal of Volcanology and Geothermal Research*, **54**, 157–176.
Sheppard, S.M.F. and Gilg, H.A. (1996) Stable isotope geochemistry of clay minerals. *Clay Minerals*, **31**, 1–24.
Sillitoe, R.H. (1993) Epithermal models: genetic types, geothermal controls and shallow features. Pp. 403–417 in: *Mineral Deposit Modeling* (R.V. Kirkham, W.D. Sinclair, R.I. Thorpe and J.M. Duke, editors), Geological Association of Canada Special Paper **40**.
Simón, M., Martin, F., García, I., Bouza, P., Dorronsoro, C., and Auilar, J. (2005) Interaction of limestone grains and acidic solutions from the oxidation of pyrite tailings. *Environmental Pollution*, **135**, 65–72.
Söylemezoğlu, S. (2010) Kuzey Batı Anadolu'da Çanakkale-Çan yöresi volkanik kayaçlarının jeolojik, petrolojik özellikleri ve evrimin araştırılması. PhD Dissertation, ITU, Fen Bilimleri Enstitüsü, İstanbul, Turkey (in Turkish).
Spell, T.L. and McDougall, I. (2003) Characterization and calibration of $^{40}Ar/^{39}Ar$ dating standards. *Chemical Geology*, **198**, 189–211.
Staudacher, T., Jessberger, E.K., Dorflinger, D., and Kiko, J. (1978) A refined ultra-high vacuum furnace for rare gas analysis. *Journal of Physics E: Scientific Instruments*, **11**, 781–784.
Steefel, C.I. and Van Cappellen, P. (1990) A new kinetic approach to modeling water-rock interaction: The role of nucleation, precursors and Ostwald ripening. *Geochimica et Cosmochimica Acta*, **54**, 2657–2677.
Stoffregen, R.E. (1987) Genesis of acid-sulfate alteration and Au-Cu-Ag mineralization at Summitville, Colorado. *Economic Geology*, **82**, 1575–1591.
Stoffregen, R.E. and Alpers, C.N. (1987) Woodhouseite and svanbergite in hydrothermal ore deposits: Products of apatite destruction during advanced argillic alteration. *Canadian Mineralogist*, **25**, 201–211.
Su, C. and Harsh, J.B. (1994) Gibbs free energies of formation at 298ºK for imogolite and gibbsite from solubility measurements. *Geochimica et Cosmochimica Acta*, **58**, 1667–1677.
Tardy, Y. (1982) Kaolinite and smectite stability in weathering conditions. Pp. 295-312, in: *Crystal Growth Processes in Sedimentary Environments* (R. Rodriguez Clemente and I. Sunagawa, editors). *Estudios Geologicos*, **38**.
Thompson, A.J.B., Hauff, P.L., and Robitaille, A.J. (1999) Alteration mapping in exploration: Application of short-wave infrared (SWIR) spectroscopy. *Society of Economic Geologists Newsletter*, **39**, 13.
Ünal, E. (2010) Genetic investigation and comparison of Kartaldağ and Madendağ epithermal gold mineralizatıon in the Çanakkale Region. M.Sc. Thesis. Middle East Technical University, Institute of Science. Ankara.
Wang, Y. (2010) Physical and chemical characteristics of the host rocks in controlling the mineralization of the Chinkuashih high-sulfidation gold–copper deposits, northeastern Taiwan. *Journal of Geochemical Exploration*, **104**, 61–68.
Yiğit, Ö. (2006) Gold in Turkey – a missing link in Tethyan metallogeny. *Ore Geology Reviews*, **28**, 147–179.
Yiğit, Ö. (2009) Mineral deposits of Turkey in relation to Tethyan Metallogeny: Implications for future mineral exploration. *Economic Geology*, **104**, 19–41.
Yiğit, Ö. (2012) A prospective sector in the Tethyan Metallogenic Belt: Geology and geochronology of mineral deposits in the Biga Peninsula, NW Turkey. *Ore Geology Reviews*, **46**, 118–148.
Yılmaz, Y. (1990) Comparison of young volcanic associations of western and eastern Anatolia formed under a compressional regime: a review. *Journal of Volcanology and Geothermal Research*, **44**, 69–87.
Yılmaz Y., Genç, S.C., Karacık Z., and Altunkaynak, S. (2001) Two contrasting magmatic associations of NW Anatolia and their tectonic significance. *Journal of Geodynamics*, **31**, 243–271.
Zotov, A., Mukhamet-Galeev, A., and Schott, J. (1998) An experimental study of kaolinite and dickite relative stability at 150–300ºC and the thermodynamic properties of dickite. *American Mineralogist*, **83**, 516–524.

(*Received 15 April 2015; revised 20 May 2016; Ms. 993; AE: P. Malla*)